

PAPER • OPEN ACCESS

The average transmitted wave in random particulate materials

To cite this article: Aristeidis Karnezis *et al* 2024 *New J. Phys.* **26** 063002

View the [article online](#) for updates and enhancements.

You may also like

- [Liouville type theorems for the 3D stationary MHD and Hall-MHD equations with non-zero constant vectors at infinity](#)
Wendong Wang and Guoxu Yang

- [Stokes flow with Oseen tensors: Stokes' law, force fields, and flow near a wall](#)
Timon Idema

- [Meshfree-based physics-informed neural networks for the unsteady Oseen equations](#)
Keyi Peng, , Jing Yue et al.

New Journal of Physics

The open access journal at the forefront of physics

Deutsche Physikalische Gesellschaft 

IOP Institute of Physics

Published in partnership
with: Deutsche Physikalische
Gesellschaft and the Institute
of Physics



OPEN ACCESS

RECEIVED
16 August 2023

REVISED
8 April 2024

ACCEPTED FOR PUBLICATION
10 May 2024

PUBLISHED
3 June 2024

Original Content from
this work may be used
under the terms of the
[Creative Commons
Attribution 4.0 licence](#).

Any further distribution
of this work must
maintain attribution to
the author(s) and the title
of the work, journal
citation and DOI.



PAPER

The average transmitted wave in random particulate materials

Aristeidis Karnezis * , Paulo S Piva  and Art L Gower 

Department of Mechanical Engineering, University of Sheffield, Sheffield, United Kingdom

* Author to whom any correspondence should be addressed.

E-mail: a.karnezis@protonmail.com

Keywords: wave scattering, multiple scattering, particulate materials, random media, ensemble averaging, Ewald–Oseen extinction theorem, Monte-Carlo simulations

Abstract

Microwave remote sensing is significantly altered when passing through clouds or dense ice. This phenomenon is not unique to microwaves; for instance, ultrasound is also disrupted when traversing through heterogeneous tissues. Understanding the average transmission in particle-filled environments is central to improve data extraction or even to create materials that can selectively block or absorb certain wave frequencies. Most methods that calculate the average transmitted field assume that it satisfies a wave equation with a complex effective wavenumber. However, recent theoretical work has predicted more than one effective wave propagating even in a material which is statistically isotropic and for scalar waves. In this work we provide the first clear evidence of these predicted multiple effective waves by using high-fidelity Monte-Carlo simulations that do not make any statistical assumptions. To achieve this, it was necessary to fill in a missing link in the theory for particulate materials: we prove that the incident wave does not propagate within the material, which is usually taken as an assumption called the Ewald–Oseen extinction theorem. By proving this we conclude that the extinction length—the distance it takes for the incident wave to be extinct—is equal to the correlation length between the particles.

1. Introduction

Most materials, at some length scale, are formed of a random configuration of smaller particles. Consider particles in powder for pharmaceuticals, grains in the sand, oil droplets in emulsions, and aggregates in solid composites. The wide number of these particulate materials, and engineering applications, make it worthwhile to develop methods to measure these materials and design them intelligently.

Background. When it comes to measurement and characterisation, the main tools are classical waves such as electromagnetic and ultrasonic or acoustic. The governing equations for these classical waves would be well-understood if the material itself was known in all its details. Unfortunately, in most cases it is impossible to know in detail the microstructure of the material because it is disordered. In these scenarios, ensemble averaging and statistical assumptions need to be used to obtain solvable systems [1–4].

How classical waves interact with particulate materials (on average) is well-understood within certain limits. In the long wavelength limit, where the particles appear small compared to the wavelength of the incident wave, it is well-understood how to calculate effective properties [5]. In the dilute limit, where there is no multiple scattering, Mie theory has led to characterisation methods such as Dynamic Light Scattering and laser diffraction resulted in a range of widely used tools ^{1,2}.

Pushing the limits. In the cases where multiple scattering is significant, and the incident wavelength is not long (compared to the microstructure), the average wave is more complex and can not be described with one single effective wavenumber [6–8]. This is especially true when using exotic pair-correlations [9, 10] and

¹ Horiba Scientific: www.horiba.com/dynamic-light-scattering.

² Malvern Panalytical: www.malvernpanalytical.com/laser-diffraction.

resonant particles [11, 12]. To push the theory to these new limits, we need to clearly understand the validity of all the assumptions made. Within this context, we aim to address two significant assumptions that currently remain unanswered discussed in more detail in the next two paragraphs.

Multiple effective wavenumbers. Most of the literature assumes there is only one effective wavenumber [13–18]. As the medium is isotropic and homogeneous (after ensemble averaging) it seems reasonable to assume that there is only one effective wavenumber k_* for waves travelling in a bulk material (i.e. no waveguide). However, two different theoretical methods [7, 19] have predicted that there exist at least two (complex) effective wavenumbers for one fixed frequency. Here we give the first clear numerical evidence of these multiple effective wavenumbers as well as demonstrate that multiple wavenumbers are triggered by particles, and frequencies, that lead to strong scattering. To clearly relate the transmitted field from numerical simulations with the transmitted wave from theoretical results, we have to first be clear on what the most general theoretical framework predicts about the transmitted field.

Incident wave extinction. It is often assumed that the incident wave does not propagate, or contribute to, the total transmitted field inside a material. This assumption is called the Ewald–Oseen extinction theorem [6, 20], and is applied more broadly than just averaged disordered or random materials. For disordered particulate material, this assumption has been derived in many different limits, including low-frequency and low particle volume fraction [21], but there are still disagreements in the literature on the exact extinction length [21], that is, the distance into the medium that the incident waves travels before vanishing. Knowing the exact extinction length is needed, for example, for experiments where the source and transmitted wave can be mixed. This doubt arises in measuring light from objects at astronomical distances [21].

In this work we are able to prove that for any particulate material geometry, frequency, and incident wave, the Ewald–Oseen extinction theorem is a result of more fundamental assumptions. Due to the proof, we can clearly demonstrate that the incident wave does not propagate further than the correlation length between the particles. That is, the extinction length is equal to the inter-particle correlation length. That means the more ordered the material is, the further the incident wave can travel before being extinct. However, this also means that the concept of the material acting as an effective medium with a single effective wavenumber only applies deeper within it, and becomes less accurate for highly ordered materials.

Microscopic extinction. The theoretical methods we use consider the scattering from all particles and take an ensemble average. This has been called the microscopic approach [2, 16, 17, 22, 23]. The microscopic approach solves the boundary conditions around every particle, and the resulting equations involve terms which satisfy the background wave equation, just like the incident wave. Cancelling these terms is often called the Ewald–Oseen extinction theorem, but it is not the same as concluding that the incident wave itself is extinct, see for example [24]. Further, this cancellation does not lead to the extinction length. We are able to connect the two approaches by showing that the boundary conditions around each particle, used in the microscopic approach, do lead to the incident wave itself being extinct, and provide an extinction length.

Monte-Carlo. There have been several studies that use Monte-Carlo methods to validate effective wave theory. Examples include comparing Monte-Carlo with: the average scattering from a sphere filled with particles [25, 26], and one effective wavenumber from the theory [27, 28]. To our knowledge, there has been no Monte-Carlo validation or evidence that more than one multiple effective wavenumber exists. Here, by using precise Monte-Carlo simulations, we provide the first clear evidence that at least two effective wavenumbers, and therefore two effective waves, are present in the transmitted field. The theoretical methods that predict these multiple effective wavenumbers make several statistical assumptions, whereas our numerical simulations make no such assumptions. They, therefore, provide a clear validation of the theoretical predictions.

Summary of the paper. In section 1.1 we provide an overview of the theory and the results of this paper.

In section 2 we discuss what the theory predicts for the average wave in a plate filled with random particles and how to easily identify when multiple wavenumbers should appear.

In section 3 we discuss our Monte-Carlo simulations, which involve simulating waves scattered from tens of thousands of particle configurations, how we verify convergence, and how we clearly demonstrate that there are scenarios where at least two effective wavenumbers appear in the transmitted field.

In section 4 we provide rigorous derivations that: the incident wave does not propagate in the particulate material, and the average transmitted wave is a sum of waves which satisfy effective wave equations. Our derivations are more general than just for a plate, they hold for a finite region, and in fact for any spatial dimension. So the proof we provide is also valid for three-dimensional materials.

1.1. Overview of the theory

Consider a harmonic incident plane-wave $u_{\text{inc}}(x) = e^{ikx}$, satisfying Helmholtz equation with wavenumber k , so that $u_{\text{inc}}(x)e^{-i\omega t}$ satisfies a scalar wave equation, where x is the distance of propagation. When this incident wave propagates through a random particulate medium, the general assumption has been that it will be replaced by one effective wave of the form:

$$\langle u(x) \rangle = A_* e^{ik_* x}, \quad (1)$$

where k_* is a complex effective wavenumber, for the fixed frequency ω , A_* is the average transmission coefficient, and $\langle u(x) \rangle$ is the ensemble average of $u(x)$ over all possible particle configurations [13–18, 29].

In the low-frequency limit, when the particles are small relative to the incident wavelength, there is substantial evidence to justify (1). But beyond the low-frequency limit, and when using more exotic pair-correlations and distributions for the particles, there is no clear consensus. Two different methods [19, 30] suggest a different form for (1) given by:

$$\langle u(x) \rangle = A_{\text{inc}} e^{ikx} + \sum_{p=1}^{\infty} A_p e^{ik_p x}, \quad (2)$$

where A_{inc} is the amplitude of the incident wave, A_p are the average transmission coefficients and k_p are complex effective wavenumbers. In the next two paragraphs we further explain the form (37).

Incident wave extinction. When A_{inc} is not zero, a part of the incident wave remains even when propagating through a random particulate. The work by Martin [24] suggests that this is the case. Assuming $A_{\text{inc}} = 0$ is called the Ewald–Oseen extinction theorem [16, 20, 22], and it is due to the scattering and absorption of energy by the random distribution of particles. Much of the literature [21] assumes this extinction happens after the incident wave has propagated a certain distance in the material. In this paper we prove that for any frequency, material geometry, particle distribution, and for two and three spatial dimensions, the incident wave is extinct ($A_{\text{inc}} = 0$ for plane-waves) at a distance equal to particle correlation length. Previous work [24, 30] did not clarify the structure of the average transmitted field.

Multiple effective wavenumbers. Each term in the sum of equation (2) represents an effective wave with a different wavenumber k_p . This is highly unusual for scalar waves at a fixed angular frequency ω . Yet, two different theoretical methods have predicted the existence of at least two ($p > 1$) complex effective wavenumbers [19, 30, 31]. The evidence for this unusual prediction, beyond just theoretical, is lacking. In this work we use highly accurate simulations and Monte-Carlo method for circular cylindrical particles to demonstrate that these extra wavenumbers are present for specific frequencies.

Average reflected field. Beyond just curiosity, these extra effective wavenumbers can have a significant effect on the average reflected, transmitted, or scattered wave from a particulate material [30, 32]. It is also far simpler to calculate the cases where there is only one dominant wavenumber [7, 13].

To understand when these multiple wavenumbers are needed, we have produced a series of phase diagrams. An example is shown in figure 1 for sound-soft particles. The regions represented by blue colours (correspond to lower values in the colour bar), require more than one effective wavenumber to accurately describe the transmitted field. For more details see figure 4 and the discussion below that figure. For example, we can see that only one wavenumber is needed for low particle volume fraction $\phi < 0.1$, with only one exception around $ka = 0.6$. The green curve in the figure shows the scattering strength of just one particle by itself. Surprisingly, we see that the frequencies at which the single particle scatters the strongest (the peaks in the green curve) are also the frequencies at which two (or more) effective wavenumbers are required, and therefore needed to accurately describe wave transmission.

In other words, strong scattering leads to multiple effective wavenumbers. A clear application where strong scattering is important is when designing materials that strongly attenuate waves (or reflect waves) at specific frequencies. The strong attenuation often occurs with strong scattering from the particles. The simplest way to design these selective materials is to analyse the effective wavenumbers, and therefore it is important to know whether there is one or more effective wavenumbers. These results, and other phase diagrams, are further discussed in section 3.1.

Average field, not intensity. In this work we only discuss the average field equation (2), which does not always represent well the average intensity $\langle u^2(x) \rangle$, or energy, of the field as shown in [33]. For some sensors, especially in the field of laser and light scattering, it is easier to measure the average intensity [34].

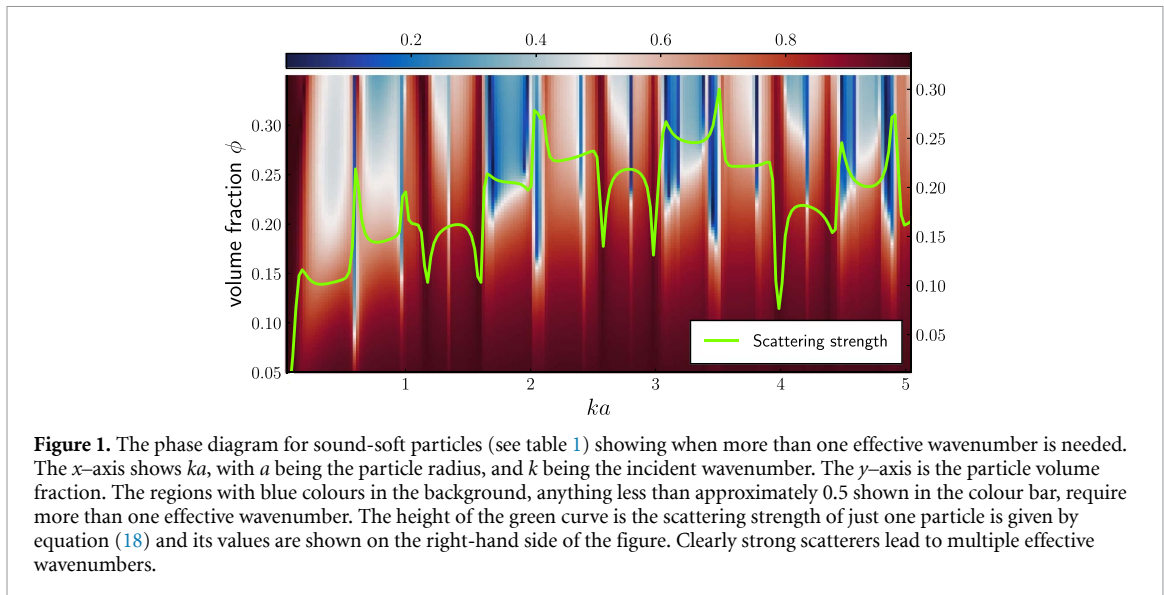


Figure 1. The phase diagram for sound-soft particles (see table 1) showing when more than one effective wavenumber is needed. The x -axis shows ka , with a being the particle radius, and k being the incident wavenumber. The y -axis is the particle volume fraction. The regions with blue colours in the background, anything less than approximately 0.5 shown in the colour bar, require more than one effective wavenumber. The height of the green curve is the scattering strength of just one particle is given by equation (18) and its values are shown on the right-hand side of the figure. Clearly strong scatterers lead to multiple effective wavenumbers.

2. A plate filled with particles

Here we show how to design a computational experiment to give clear evidence that there are at least two effective wavenumbers, for the same frequency ω , despite the medium being isotropic and homogeneous. Our experiment will use a robust numerical method based on high-fidelity Monte-Carlo simulations for two-dimensional disks. See appendix A for details.

To describe the material, let \mathcal{P}_j be the disk occupied by the j th particle, as represented by the circles in figure 2 and shown in more detail in figure 10. Let $\mathcal{P} = \cup_j \mathcal{P}_j$ be the union of all particles. For simplicity we consider circular particles of equal size. In other words, using standard set-builder notation:

$$\mathcal{P}_j = \{\mathbf{r} \in \mathbb{R}^2 : |\mathbf{r} - \mathbf{r}_j| < a\}, \quad (3)$$

where a is the radius of the particle, centred at \mathbf{r}_j , and $|\mathbf{x}|$ is the length of the vector \mathbf{x} .

The particles are restricted inside the plate geometry \mathcal{R} , given by:

$$\mathcal{R} = \left\{ (x, y) \in \mathbb{R}^2 : 0 \leq x \leq W, -\frac{H}{2} \leq y \leq \frac{H}{2} \right\}, \quad (4)$$

where W is the width and H is the height of the plate as shown in figure 2.

The total field $u(\mathbf{r})$ satisfies a Helmholtz equation which depends on whether \mathbf{r} is inside a particle or not:

$$\nabla^2 u(\mathbf{r}) + k^2 u(\mathbf{r}) = 0, \quad \text{for } \mathbf{r} \in \mathcal{R} \setminus \mathcal{P}, \quad (5)$$

$$\nabla^2 u(\mathbf{r}) + k_o^2 u(\mathbf{r}) = 0, \quad \text{for } \mathbf{r} \in \mathcal{P}, \quad (6)$$

where $k = \omega/c$ and $k_o = \omega/c_o$ are the real wavenumbers of the background and particles respectively. The scalars c and c_o are, respectively, the wavespeeds in the background and particles.

The simplest scenario to numerically check for effective waves is for planar symmetry. As in this case each frequency has only one mode: the plane-wave. An alternate approach to validate the theory of effective waves is to do Monte-Carlo simulations of particles within a sphere [35], or circular particles within a circle [36]. These have the added benefit of requiring a finite computational domain, though the transmitted fields are more complex.

To simulate planar symmetry, i. e. plane-waves, we fill a plate region with a configuration of randomly distributed cylindrical particles, as shown in figure 2. The particles are identical, except for their positions.

2.1. Effective waves for planar symmetry

Here we summarise the results of the theory for plane-wave symmetry. The results here will be compared with a Monte-Carlo method detailed in section 3.

We consider an incident plane-wave of the form:

$$u_{\text{inc}}(x) = e^{ikx}, \quad (7)$$

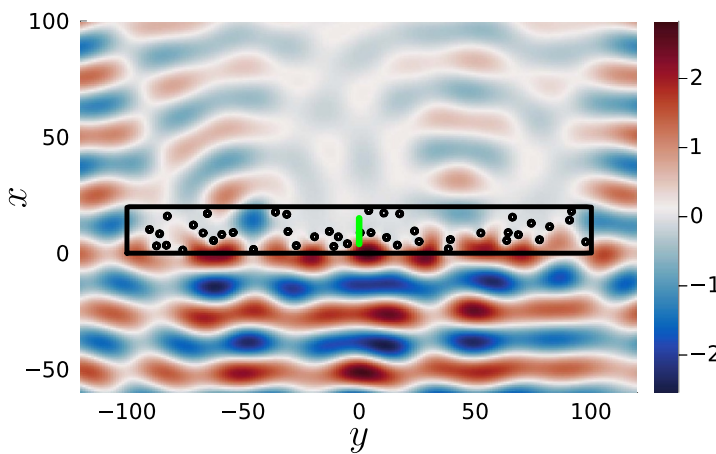


Figure 2. Scattering of an incident plane-wave approaching from the left, onto one specific configuration of randomly distributed circular cylinders (or particles) Λ . The density and wavespeed of the background medium are given by arbitrary values represented by ρ and c respectively. The particles with radius $a = 1.2$ are considered strong scatterers with density $\rho_o = 0.3\rho$ and wavespeed $c_o = 0.3c$. To perform this simulation we choose a dimensionless frequency $ka = 0.96$ and a particle volume fraction $\phi = 8\%$. The solid black line depicts the plate boundary while the green line shows where the field is measured. The simulation directly solves the governing equations [15].

and consider particles in a plate region \mathcal{R} with an infinite height, whereas figure 2 shows a truncated plate with a finite height.

The theoretical methods consider an ensemble average of the total field u . To achieve this, we describe one configuration of particles with:

$$\Lambda = (\mathbf{r}_1, \mathbf{r}_2, \dots, \mathbf{r}_J), \quad (8)$$

where \mathbf{r}_j is the centre position of the particle \mathcal{P}_j . Naturally, the field u depends on the particle positions. To make this explicit we use $u(x; \Lambda)$.

Next, to calculate the ensemble average, we need to define the probability of all possible particle configurations. To do this, we introduce the joint probability density given by $p(\Lambda)$. For a brief overview on the probability density function p , see [7, 14, 37]. The theoretical methods then calculate and predict the ensemble average defined by:

$$\langle u(x) \rangle := \int u(x; \Lambda) p(\Lambda) d\Lambda, \quad (9)$$

where the integral is over all possible particle positions, and the fields depend only on the spatial position x as we are considering planar symmetry.

It is widely assumed that the average $\langle u(x) \rangle$ satisfies a Helmholtz equation with a unique effective complex wavenumber k_* [13–18]. In section 4.1 we prove that $\langle u(x) \rangle$ is a sum of several effective waves, but only when x is deep enough within the material. To define what ‘deep enough’ means we need to introduce the particle pair-correlation.

Pair-correlations. An important feature of randomly distributed particles is their pair-correlation function, given by:

$$g(\mathbf{r}_1 - \mathbf{r}_2) = \frac{p(\mathbf{r}_1, \mathbf{r}_2)}{p(\mathbf{r}_1)p(\mathbf{r}_2)}. \quad (10)$$

Essentially, $g(\mathbf{r})$ measures the probability of finding another particle at a distance \mathbf{r} from a given reference particle. In other words, $g(\mathbf{r})$ describes how particle density varies as a function of distance from a reference particle in each possible configuration of particles. For an example, see figure 3.

We assume that particles are distributed both homogeneously and isotropically, which leads to $g(\mathbf{r}_1 - \mathbf{r}_2) = g(|\mathbf{r}_1 - \mathbf{r}_2|)$ for an infinite number of particles.

For a disordered or random configuration of particles we have that:

$$g(|\mathbf{r}_1 - \mathbf{r}_2|) = \begin{cases} 0 & \text{if } |\mathbf{r}_1 - \mathbf{r}_2| \leq a_{12}, \\ 1 & \text{if } |\mathbf{r}_1 - \mathbf{r}_2| \geq b_{12}, \end{cases} \quad (11)$$

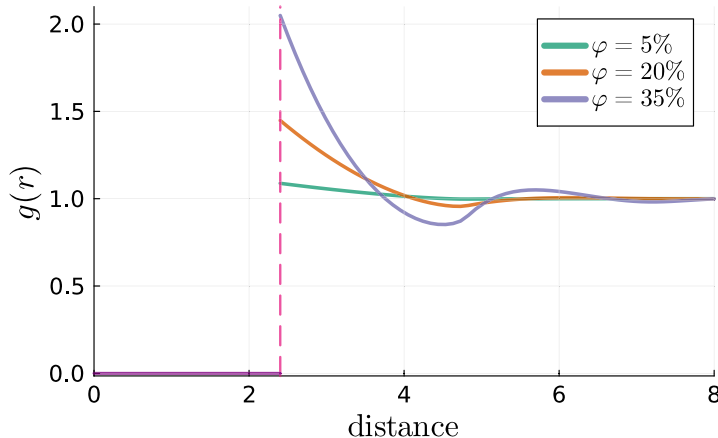


Figure 3. The Percus–Yevick approximation is a pair-correlation that represents particles that are uniformly randomly placed, except particles do not overlap. That is, particles do not attract or repel each other. The particle radius $a = 1.2$ and ϕ is the particle volume fraction.

where $b_{12} \geq a_{12} > 2a$. The distance a_{12} is the minimum allowed distance between the particles while b_{12} is called the correlation length. For the region $a_{12} \leq |\mathbf{r}_1 - \mathbf{r}_2| \leq b_{12}$ the pair-correlation can take any values for our calculation below, though we expect $g(\mathbf{r})$ to be continuous in \mathbf{r} . In this work we use two different pair-correlations. The first, and the simplest, is called *Hole-Correction*, which assumes that $b_{12} = a_{12}$. The second is called the *Percus–Yevick* approximation, which more accurately approximates the pair-correlation for particles that are distributed according to a uniform random probability, except no two particles can overlap [17, 38–40]. We use the results from [41] to obtain Percus–Yevick for disks. Figure 3 shows the Percus–Yevick distributions for several different particle volume fractions ϕ .

For disordered media we have that $g(r) \rightarrow 1$ as $r \rightarrow \infty$. That is, particles become uncorrelated as they are further apart. To prove that $\langle u(x) \rangle$ is a sum of effective waves we need a slightly stronger assumption: that there is a distance b_{12} at which particles are completely uncorrelated as used in equation (11). For more details on pair-correlations see [39, 40].

Effective plane-waves. By having a length b_{12} at which particles become uncorrelated, we demonstrate in section 4.1 that for an infinite plate geometry ($H \rightarrow \infty$ in equation (4)) filled with particles:

$$\langle u(x) \rangle = \sum_{p=1}^P (A_p^+ e^{ik_p x} + A_p^- e^{-ik_p x}) \quad \text{for } \left| x - \frac{W}{2} \right| < \frac{W}{2} - b_{12} - a, \quad (12)$$

where we used planar symmetry as shown in [7]. The A_p^\pm are complex amplitudes, the k_p are the complex effective wavenumbers, and P is the number of effective wavenumbers. There is an infinite number of wavenumbers P , but according to theoretical calculations only a few are needed for accurate results. For a detailed discussion on these multiple effective wavenumbers see [30, 32].

The dispersion equation. To calculate the wavenumbers k_p we use the dispersion equation appearing in [14, 30, 32]. The assumptions needed to arrive at this dispersion equation are shown in section 4. To summarise, the k_p are determined by solving:

$$\det \mathbf{M}(k_\star) = 0, \quad \text{with } M_{nn'}(k_\star) = \delta_{nn'} + 2\pi n T_n [\mathcal{N}_{n'-n} - \mathcal{G}_{n'-n}], \quad (13)$$

where

$$\mathcal{N}_\ell = \frac{1}{k_\star^2 - k^2} (ka_{12} H_l'(ka_{12}) J_l(k_\star a_{12}) - k_\star a_{12} H_l(ka_{12}) J_l'(k_\star a_{12})), \quad (14)$$

$$\mathcal{G}_\ell = \int_{a_{12}}^{b_{12}} J_\ell(k_\star r) H_\ell(kr) (g(r) - 1) r dr, \quad (15)$$

and the term n is the average number of particles per area, $r = |\mathbf{r}|$, $\delta_{nn'}$ is the Kronecker delta, and H_ℓ is the Hankel function of the first kind, while J_ℓ is the Bessel function. The term T_n is the T-matrix which

determines how one particle scatters waves by itself. For circular homogeneous particles in acoustics we have that:

$$T_n = -\frac{\gamma J'_n(ka) J_n(k_o a) - J_n(ka) J'_n(k_o a)}{\gamma H'_n(ka_o) J_n(k_o a) - H_n(ka) J'_n(k_o a)}, \quad (16)$$

where $\gamma = \rho_o c_o / \rho c$ and $k_o = \omega / c_o$, with ρ_o being the mass density of the particles and c_o being the wavespeed within the particles.

There are infinitely many k_* which solve $\det M(k_*) = 0$. We denote these solutions as k_1, k_2, \dots . The main objective of our Monte-Carlo simulations is to check if the theoretical predictions of the wavenumbers k_p are accurate, and to clearly demonstrate that there is more than one effective wavenumber appearing in the Monte-Carlo results. Before doing this, let us first explore the effective wavenumbers predicted by solving the dispersion equation (13).

Effective wavenumbers. We want to identify when the dispersion equation (13) predicts that there is more than one effective wavenumber that has a significant contribution to the average transmitted wave. It is important to understand when this occurs, as it is far simpler to calculate the average field when there is only one effective wavenumber [7, 30].

Most of the scientific community at present is also not aware that more than one effective wavenumber can be excited [2, 6, 15], for just one scalar wave. So we will identify for which parameters we can run a Monte-Carlo simulation, as detailed in section 3, to find clear numerical evidence of multiple effective wavenumbers.

According to theoretical results, only one effective wavenumber k_1 is needed when $\text{Im } k_1 \ll \text{Im } k_p$ for $p = 2, 3, \dots$. In any other case, more than one effective wavenumber can be excited and contribute to the average transmission [30, 32]. Though we note that the form of the incident wave and the geometry of the material also affects how the wavenumbers are excited [7].

The first step is to sweep the parameter space by varying the frequency ω and particle volume fraction ϕ , and for each value calculate the effective wavenumbers k_p by solving (13). We do this for both sound-hard and sound-soft particles by changing ρ_o and c_o in equation (16). The two main particle properties used are shown in table 1. Next, based on the results shown in [30, 32], we can estimate where more than one effective wavenumber is excited by plotting a heatmap where the colour is given by:

$$\text{colour} = \left| \frac{\text{Im } k_2}{\text{Im } k_1} - 1 \right|. \quad (17)$$

We note that as the vertical stripes in figure 4 do not depend on the particle volume fraction, they must be related to the properties of a single particle. After some experimentation we find that the measure equation (17) is closely related to the scattering strength of a single particle, given by:

$$\text{Scattering strength} = \sqrt{\sum_n |T_n|^2}, \quad (18)$$

where T_n is the T -matrix given by equation (16) for acoustics.

The results of sweeping over frequency and particle volume fraction are shown in figure 4. We call these figures phase diagrams, as we see sudden shifts from only one effective wavenumber to two or more wavenumbers. The regions with blue shading correspond to cases where the value of equation (17) is low (below 0.5), so more than one effective wavenumber is excited. Conversely, the regions with red shading (above 0.5) are where only one effective wavenumber is excited. The regions with lighter colours are closer to the transition between one or multiple excited wavenumbers. The green curves shown on top of the phase diagrams are the scattering strength for just one particle. Clearly we see that a large scattering strength leads to more than one effective wavenumber, which is an important observation, as calculating equation (18) is far simpler than calculating the wavenumbers k_p .

The phase diagrams in figure 4 show a large region of the parameter space, but to see in more detail when two or more effective wavenumbers are needed it helps to plot the imaginary parts of the wavenumbers k_p against frequency, which we do in figure 5 for a particle volume fraction of 25%. For sound-soft particles (figure 5(a)), there are many frequencies ka where two or even three effective wavenumbers have a similar imaginary part, meaning that these wavenumbers can be excited. For some regions in the plot, it is very difficult to determine which point belongs to each different k_p curve. In contrast, for sound-hard particles (figure 5(b)), there is only one effective wavenumber that can be easily excited, as there is one clear curve representing k_1 , which has a significantly lower imaginary part than all the others.

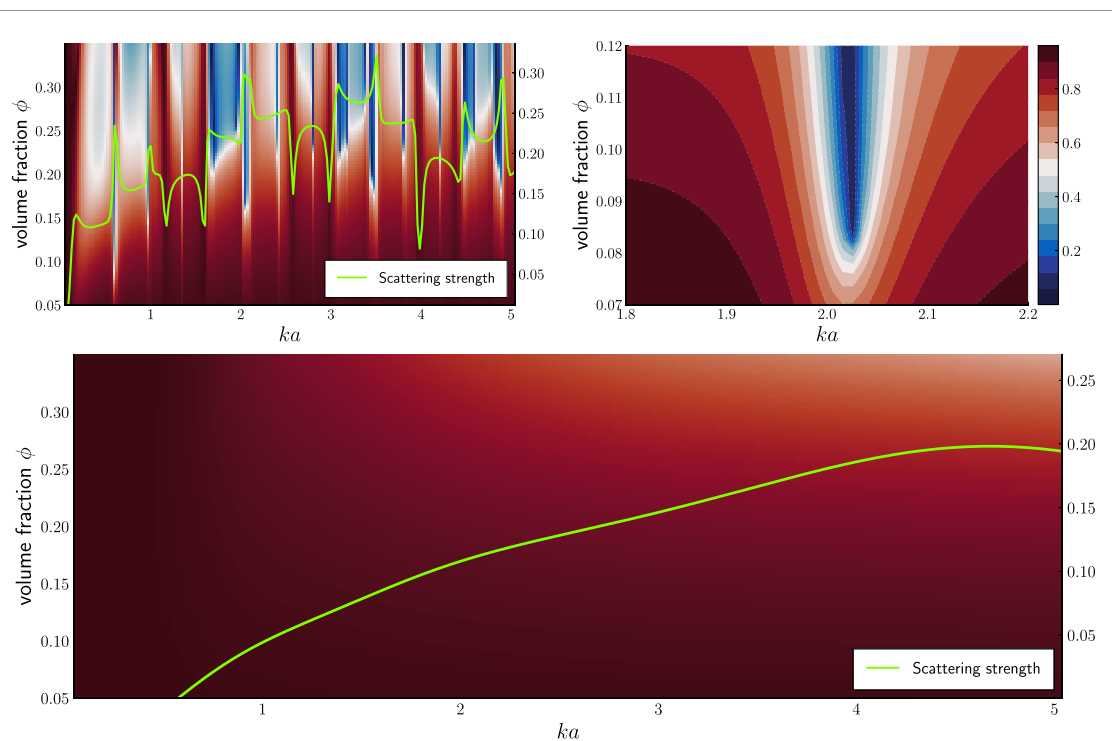


Figure 4. The phase diagrams showing when more than one effective wavenumber is needed. The top two diagrams are for sound-soft particles and the bottom diagram is for sound-hard particles with properties shown in table 1. The colour is given by equation (17) where the blue colours (those below 0.5 shown in the colour bar) indicate that more than one effective wavenumber can be excited. The green curve shows the scattering strength of just one particle and is given by equation (18). The scattering strength was computed with 5 modes of the T-matrix in both graphs.

Table 1. Shows the two main particle properties used for the numerical results. Note that sound-soft (sound-hard) particles are strong (weak) scatterers.

	Density	Wavespeed
Background medium	ρ	c
Sound-soft particles	$\rho_o = 0.3 \rho$	$c_o = 0.3 c$
Sound-hard particles	$\rho_o = 10 \rho$	$c_o = 10 c$

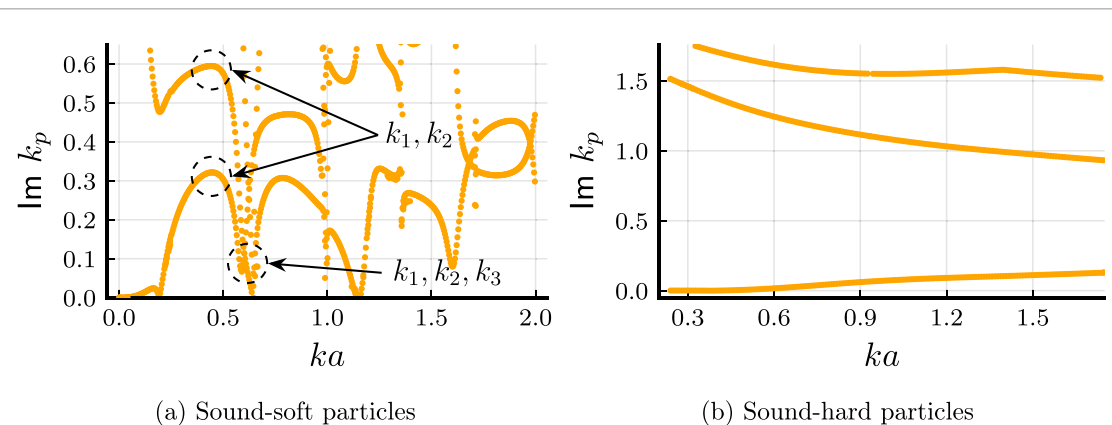


Figure 5. Depicts the imaginary part of the wavenumbers k_p with respect to the non-dimensional frequency ka . Wavenumbers in the y-axis are represented in units such that $a = 1.2$ is dimensionless. We only show the three wavenumbers with the smallest imaginary parts as these are the only ones which make a significant contribution to the average wave. The lowest curve represents k_1 , which is the easiest to excite. The particles occupy 25% of the material in each case and their properties for sound-soft and hard particles are shown in table 1.

In the next section, we use the results presented in figure 5 to identify specific scenarios where performing a Monte-Carlo simulation would be appropriate. This will allow us to verify whether the predictions of more than one effective wavenumber are indeed accurate.

3. The Monte-Carlo simulation

A simple way to approximate the average field (9) is to perform a simulation for each particle configuration and then take an average over all configurations. As we are focusing on uniformly distributed particles, the probability density $p(\Lambda)$ is a constant if particles do not overlap, and $p(\Lambda) = 0$ if any two particles do overlap. This allows us to numerically approximate the ensemble average:

$$\langle u(\mathbf{r}; \Lambda) \rangle = \frac{1}{S} \sum_{s=1}^S u(\mathbf{r}; \Lambda_s), \quad (19)$$

where each Λ_s is one randomly sampled configuration of particles within the plate that depends on the parameter s . That is, we first create a configuration of particles Λ_s , then simulate the scattered waves $u(\mathbf{r}; \Lambda_s)$, and then we repeat this process for S configurations of particles, until the average in equation (19) converges. As mentioned in previous sections, $\langle u(\mathbf{r}; \Lambda) \rangle$ should converge to a sum of plane-waves as shown by equation (12).

The setup for our Monte-Carlo simulations is shown in figure 2 (note the x -axis is the vertical axis in the figure), and we used an incident wave of the form $u_{\text{inc}}(x) = e^{ikx}$. To calculate the field $u(\mathbf{r}; \Lambda_s)$ for each configuration we use a multipole expansion for each particle, together with addition translation matrices, to solve the boundary conditions [15]. Specifically, we solve [30, equation (2.9)] for each s , calculate equation (19) and evaluate the field at $\langle u(x, 0; \Lambda_s) \rangle$ with the x values satisfying the condition at equation (12). This method accurately approximates the exact solution when increasing the truncation order of the multipole expansion until reaching convergence.

An initial numerical investigation revealed that it was computationally feasible to simulate a finite number of particles within the region $0 \leq x \leq 20$, so the width of plate $W = 20$ and height $H = 400$. For details on the methodology of our Monte-Carlo simulations, see appendix A.

3.1. The Monte-Carlo results

Based on the results of the previous section, we choose several cases to simulate the average field with a Monte-Carlo method. We want to identify cases where two or even three wavenumbers can be excited for frequencies as low as possible, because increasing the frequencies lead to a significantly larger computational cost for the Monte-Carlo simulations. This is why we only performed Monte-Carlo simulations for three different frequencies, beyond the low-frequency limit. See appendix A for details, and descriptions on computational cost.

One effective wavenumber. From figure 5(b) we see that for sound-hard particles there is a broad range of frequencies where there is only one effective wavenumber with an imaginary part which is far smaller than all others. This means that it is easy to excite this wavenumber, but very difficult to excite the others. This message is also confirmed by the phase diagram shown in figure 4. To verify there is only one effective wavenumber, we perform Monte-Carlo simulations for $ka = 0.36$ for sound-hard particles, and fit equation (12). The results shown in figure 6(b) confirm that there is only one wavenumber present in the Monte-Carlo simulations.

There is a small discrepancy between the effective wavenumbers from the dispersion equation (13) and the fitted effective wavenumbers, which could be due to errors introduced in the Monte-Carlo simulations due to truncating an infinite region.

On the other hand, for sound-soft particles we see from figure 5(a) that only for lower frequencies $0 \leq ka \leq 0.2$, only one effective wavenumber with a smaller imaginary part exists. Monte-Carlo simulations, shown in figure 6(a), confirm that there is only one effective wavenumber as predicted by the theory.

In figure 6(a), we expect the imaginary part of the effective wavenumber to be close to zero because we are in the low-frequency and low volume fraction limit [7]. Having a negative imaginary part for the Monte-Carlo wavenumber is likely just due to small numerical errors. That is, if instead we enforced that the imaginary part of Monte-Carlo wavenumber was zero, then we would still obtain a fitting error for (A.3) which is smaller than the standard error of the mean of the Monte-Carlo simulations.

Fitting for several effective wavenumbers. Increasing the frequency for sound-soft particles leads to many frequencies where two, or more, effective wavenumbers have a lower imaginary part. For example, for $0.25 < ka < 0.63$ there are multiple wavenumbers with a smaller imaginary part, which means it is possible to excite two, or even three effective wavenumbers in this frequency range. To exemplify, we choose two different frequencies to perform Monte-Carlo simulations: (1) $ka = 0.36$, where we aim to excite two effective wavenumbers, and (2) $ka = 0.62$ where we aim to excite three effective wavenumbers.

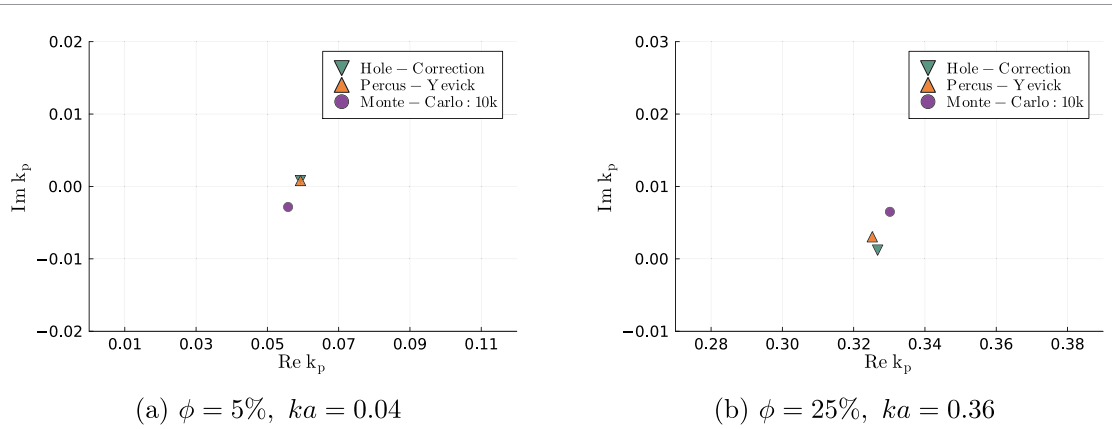


Figure 6. The figure on the left shows the behaviour of sound-soft particles in the low-frequency and low volume fraction regime, whereas the figure on the right demonstrates the properties of sound-hard particles. The specific characteristics of these particles are detailed in table 1. Wavenumbers k_p are represented in units such that $a = 1.2$ is dimensionless. Both figures depict scenarios where the dispersion equation (13) predicts there is only one effective wavenumber k_p with a lower imaginary part, and therefore this is the only wavenumber that can be excited. The green and red triangles represent effective wavenumbers predicted by equation (13) when using either the Hole-Correction or Percus-Yevick pair-correlation. The purple dotted points represent the effective wavenumber which best fits the Monte-Carlo simulations when using equation (12).

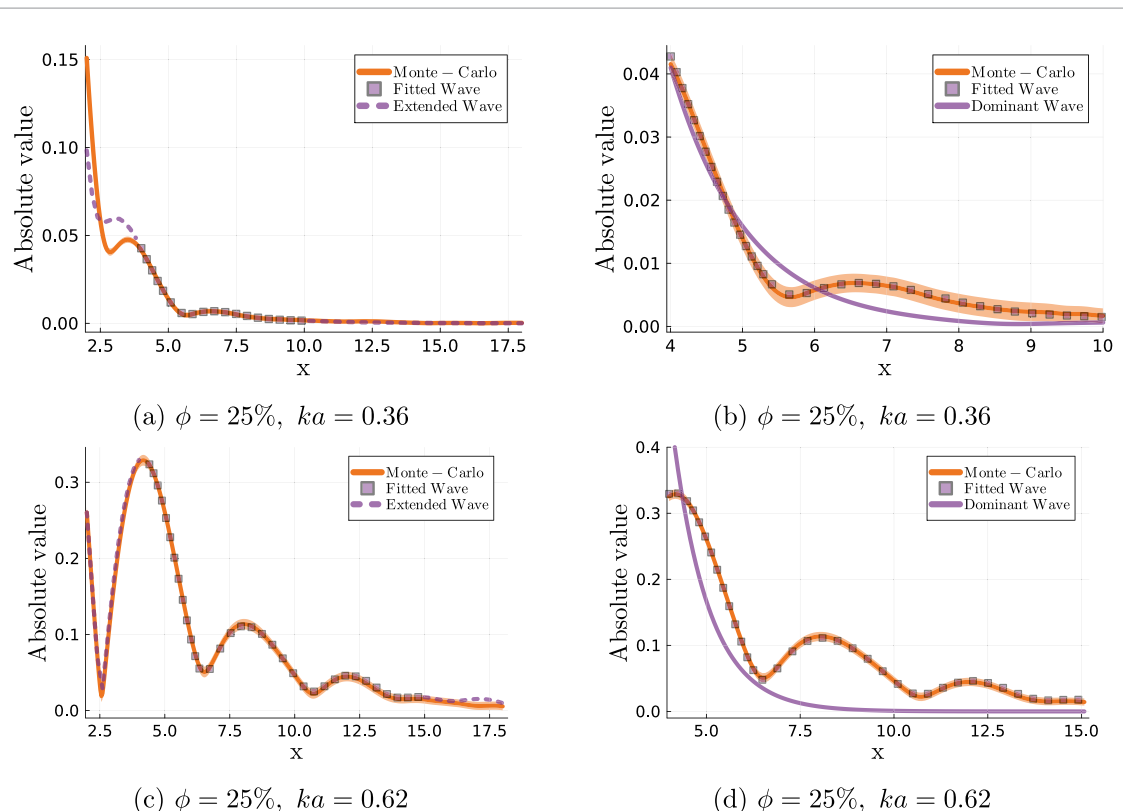
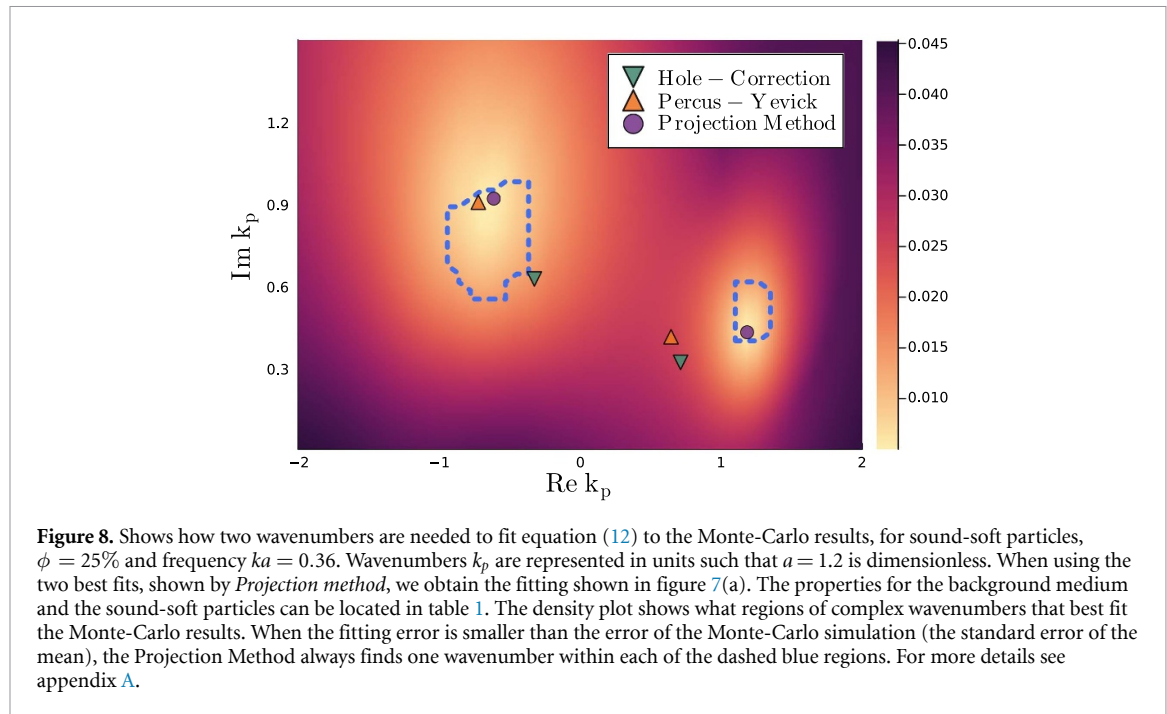


Figure 7. The graphs compare the average field from a Monte-Carlo simulation for particles in a plate, as shown in figure 2, with two types of fitted waves, the *Dominant Wave* and the *Fitted Wave*. The non-dimensional frequency ka and volume fraction ϕ used are shown below each figure, the particle radius is $a = 1.2$ and the properties for the background medium and the sound-soft particles can be found in table 1. The key parameters for simulating the scattering of waves in a plate filled with particles are discussed in appendix A.

The simulations were run until the standard error of the mean reaches around, or below, 1% relative error. The shaded region around the orange lines in figures 7 and 9(a), (c) represent the standard error of the mean. See appendix A for details on these Monte-Carlo simulations. In figure 7 we compare the Monte-Carlo simulations with two methods: the *Dominant Wave* and the *Fitted Wave*.

The Dominant Wave is given by equation (12) with just one effective wavenumber (with $P = 1$), where the amplitudes A_1^+, A_1^- , and effective wavenumber k_1 are determined by a best fit to the Monte-Carlo data.



This approach is widely used, but it fails to fit to the data in regions where more than one effective wavenumber is present. We demonstrate this in figures 7(b) and (d) for $ka = 0.36$ and $ka = 0.62$ respectively.

The Fitted Wave is given by equation (12) with $P > 1$. That is, we accept that there are multiple effective wavenumbers and determine their amplitudes and wavenumbers by a best fit to the Monte-Carlo data. We first try $P = 2$, and only increase to $P = 3$ if the fitting error is not small enough. For $ka = 0.36$, shown in figure 7(b) we obtained a small fitting error with $P = 2$, while for $ka = 0.62$, shown in figure 7(d), we needed $P = 3$ to obtain a smaller fitting error. In figures 7(a) and (c) we extend the Fitted Wave beyond the data that was used for the fitting and have called this extension the *Extended Wave*. The Extended Wave is expected not to perfectly match with the Monte-Carlo field when approaching to $x = 0$ due to a boundary layer which contains many effective wavenumbers [30, 32]. The presence of this boundary layer, and our theoretical results in section 4, have all guided how best to perform, and fit to, the Monte-Carlo results as discussed in appendix A.

Avoid overfitting. Having an accurate fit does not necessarily give strong evidence that equation (12) is correct. This is especially true for higher frequencies where the Monte-Carlo simulation has a higher standard error of the mean, shown by the shaded yellow region. A larger standard error means that there is a range of effective wavenumbers which can fit this data, and still be closer to the Monte-Carlo results than the standard error. Further, fitting a sum of plane-waves, such as shown by equation (12), can lead to over-fitting when using too many wavenumbers, and even become ill-posed. We explain more details on this in the Monte-Carlo methodology in appendix A.

To verify that we avoid over-fitting, and check if small changes in the field lead to large changes in the fitted wavenumbers, we develop a method, called the projection method, which fits equation (12) for all possible combinations of the effective wavenumbers in a region. Details are given in appendix A.

At least two effective wavenumbers. The result of fitting for two effective wavenumbers for $ka = 0.36$ is shown in figure 8. The main conclusion is that this is the first clear evidence that there are two complex effective wavenumbers by using Monte-Carlo simulations which are highly accurate. In more detail: the figure shows that there are two separate effective wavenumbers: one within the blue dashed curve on the left and the other, necessarily, within the blue dashed curve on the right. Wavenumbers within these dashed regions lead to fitting errors which are smaller than the error committed by the Monte-Carlo simulation. We also see the dispersion equation (13), together with the Percus-Yevick pair-correlation, predicts at least one wavenumber within the blue dashed curve. The predicted wavenumbers when using the Hole-Correction pair-correlation are also shown. The dispersion equation (13) predicts an infinite number of effective wavenumbers, so we present only the two wavenumbers with the smallest imaginary part.

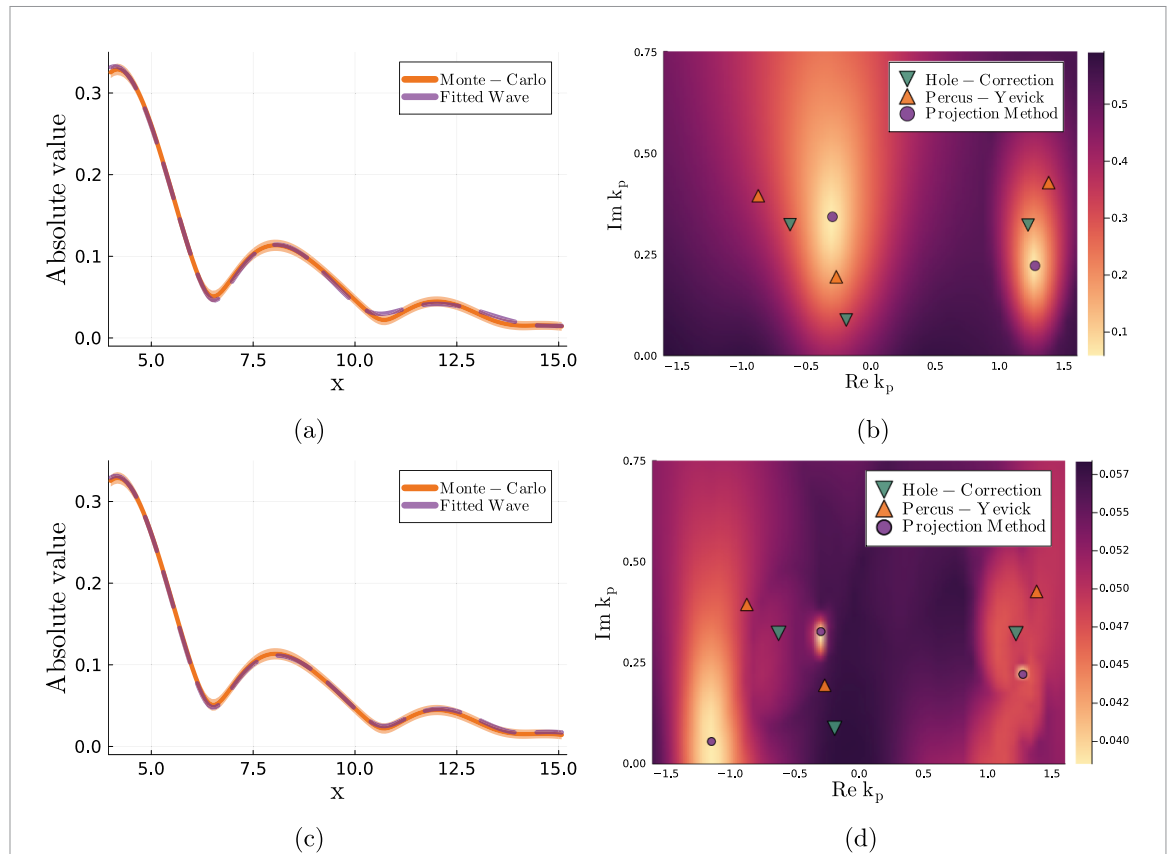


Figure 9. The top two graphs show the result of using two effective wavenumbers in equation (12) to fit the Monte-Carlo results for sound-soft particles, $\phi = 25\%$ and frequency $ka = 0.62$. Wavenumbers k_p are represented in units such that $a = 1.2$ is dimensionless. The properties for the background medium and the sound-soft particles can be found in table 1. (b) shows a density plot over the effective wavenumbers, with light regions indicating that those wavenumbers better fit the data. However, all possible choices of two wavenumbers lead to fitting errors which are greater than the standard error of the mean of the Monte-Carlo simulations. The two wavenumbers with the best fit are denoted by the *Projection method*, and lead to the field shown in (a). The bottom two graphs use three effective wavenumbers in equation (12) to fit the Monte-Carlo results. In this case, we find 4 sets of wavenumbers, all close to each other, that have a fitting error less than the standard error of the mean. The result of using the three wavenumbers with the best fit is shown in (c). However, in (d) we see that there are many choices for the wavenumbers which lead to small fitting errors. In particular, the Projection method wavenumber with the smaller imaginary part is sensitive to small changes in the Monte-Carlo results.

Three effective wavenumbers. Figure 9 shows in steps our attempt to identify three effective wavenumbers for $ka = 0.62$ predicted by equation (13). For both Hole-Correction and Percus-Yevick predictions, see figure 9(d). The summary is that the amplitude A_3 for the third wavenumber in equation (12) is too small, $|A_3| \approx 0.004$, and as a result, we can not reliably say whether the Monte-Carlo simulations show that there are indeed three effective wavenumbers. This is because the expected errors from the Monte-Carlo simulation are on the order of around 0.003 for the fitted wave. However, we do conclude again that one effective wavenumber is not enough, at least two are needed.

In more detail, the top two graphs of figure 9 show the result of fitting equation (12) with $P = 2$ to the Monte-Carlo results. Although there are clearly choices of two wavenumbers which fit the data well, there are no possible choices which lead to fitting errors that are less than the standard error of the mean, as shown in figure 9(a) which uses the two wavenumbers with the best fit. The bottom two graphs figure 9 show how the fitting errors decrease when adding a third wavenumber, i.e. using $P = 3$ in equation (12). By using $P = 3$, instead of $P = 2$, the fitting error decreased from 6% to 3.8%. Although the fitting error does decrease to below the standard error of the mean, it is only a small decrease, and close to the errors inherent in the Monte-Carlo data. We note that the two Projection Method wavenumbers shown in figure 9(b) are equal to two of the Projection Method wavenumbers shown in figure 9(d).

4. Deducing the average transmitted wave

In [7, 30, 32] the authors demonstrated that there exist several effective wavenumbers, however, it was not clear how these appear in the average transmitted field. Taking inspiration from [24], the average transmitted field should be a sum of waves, each with a different effective wavenumber. In this section we demonstrate this for any incident field and material geometry.

We use the same notation given in [7] and, as a first step, combine the methods shown in [7, 24] to demonstrate that the average transmitted field is a sum of the incident field plus several effective fields. We will later prove that the amplitude of this incident field is zero. In section 3 we numerically validate these theoretical findings, see for example figure 7.

We note that although the paper [7] is written for three-dimensional particles, the results that lead up to [7, section 5] are valid for any dimension as long as we appropriately define the spherical waves u_n and v_n and the translation matrices $\mathcal{V}_{nn'}$ and $\mathcal{U}_{nn'}$. In the case of two dimensions and scalar waves these terms are:

$$v_n(\mathbf{kr}) = J_n(kr) e^{im\theta}, \quad u_n(\mathbf{kr}) = H_n(kr) e^{im\theta}, \quad (20)$$

$$\mathcal{V}_{nn'}(\mathbf{r}) = v_{n-n'}(\mathbf{r}), \quad \text{and} \quad \mathcal{U}_{nn'}(\mathbf{r}) = u_{n-n'}(\mathbf{r}), \quad (21)$$

where J_n and H_n are the Bessel function and Hankel function of the first kind, and (r, θ) are the polar coordinates of \mathbf{r} . In our calculations, we will use the general notation rather than substitute the specific form for the two dimensions as shown in equation (21). This way, the proofs we present are valid for any dimension.

For just one configuration of particles, the way we represent the total field $u(\mathbf{r})$ depends on whether \mathbf{r} is inside a particle or not. We choose to write the field in the form [24, 42, 43]:

$$u(\mathbf{r}) = \begin{cases} u_{\text{inc}}(\mathbf{r}) + u_{\text{sc}}(\mathbf{r}), & \text{for } \mathbf{r} \in \mathcal{R} \setminus \mathcal{P}, \\ u_{\text{in}}^j(\mathbf{r}), & \text{for } \mathbf{r} \in \mathcal{P}_j, \end{cases} \quad (22)$$

where $u_{\text{inc}}(\mathbf{r})$ is the incident wave, $u_{\text{sc}}(\mathbf{r})$ is a sum of all the scattered waves, and $u_{\text{in}}^j(\mathbf{r})$ is the field inside particle j . We use \mathcal{P}_j to denote the region occupied by particle j , whereas $\mathcal{P} = \cup_j \mathcal{P}_j$ is the union of all particles. See figure 10 for an illustration.

The sum of the scattered waves $u_{\text{sc}}(\mathbf{r})$, shown in (22), is given by:

$$u_{\text{sc}}(\mathbf{r}) = \sum_{j=1}^J u_{\text{sc}}^j(\mathbf{r}), \quad \text{where} \quad u_{\text{sc}}^j(\mathbf{r}) = \sum_n f_n^j u_n(\mathbf{kr} - \mathbf{kr}_j). \quad (23)$$

The field inside the j -th particle can be written in terms of a regular radial waves expansion:

$$u_{\text{in}}^j(\mathbf{r}) = \sum_n b_n f_n^j v_n(k_o \mathbf{r} - k_o \mathbf{r}_j), \quad (24)$$

where

$$b_n = \frac{T_n H_n(ka) + J_n(ka)}{T_n J_n(k_o a)}, \quad (25)$$

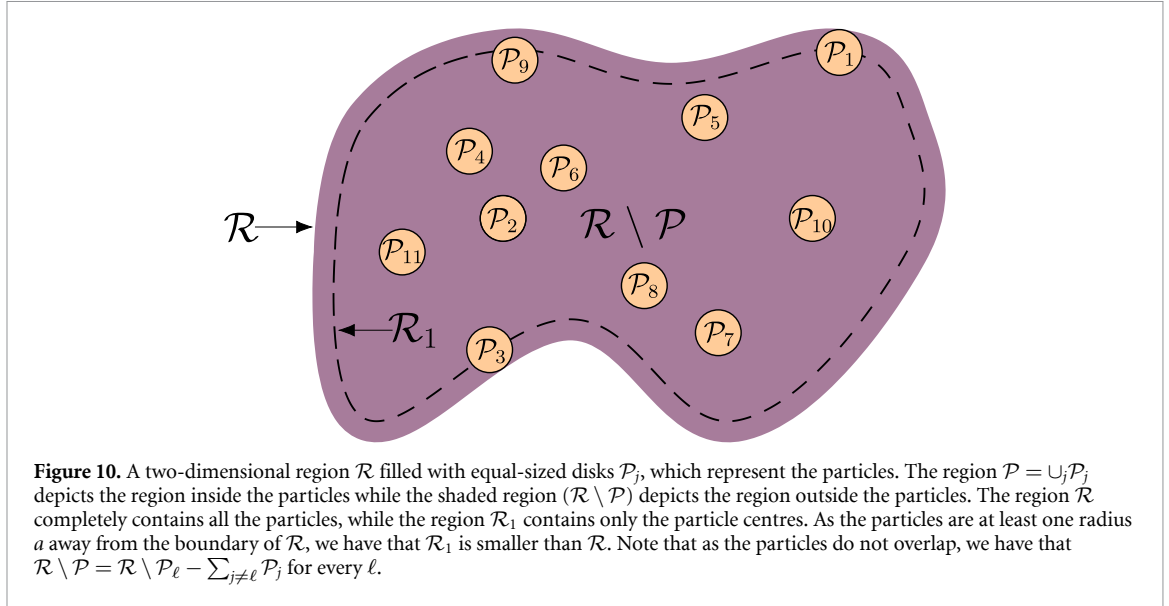
and, as a reminder, $k_o = \omega/c_o$ and T_n is given by equation (16). The coefficients in equation (25) describe how the internal structure of the particles affects the wave. For a light introduction on the T -matrix and multiple scattering see [44, 45].

The ensemble average of any field f , and the conditional ensemble average, is defined as:

$$\langle f \rangle = \int_{\mathcal{R}_1^J} f p(\mathbf{r}_1, \dots, \mathbf{r}_J) d\mathbf{r}_1 \cdots d\mathbf{r}_J, \quad (26)$$

$$\langle f \rangle(\mathbf{r}_1) = \int_{\mathcal{R}_1^{J-1}} f p(\mathbf{r}_2, \dots, \mathbf{r}_J | \mathbf{r}_1) d\mathbf{r}_2 \cdots d\mathbf{r}_J. \quad (27)$$

Here \mathcal{R}_1^J denotes that the integration domain of all J integrals is \mathcal{R}_1 , which corresponds to the region containing only the particle centres. The probability density function $p(\mathbf{r}_1, \mathbf{r}_2, \dots, \mathbf{r}_J)$ represents the



likelihood of having particles centred at $\mathbf{r}_1, \mathbf{r}_2, \dots, \mathbf{r}_J$, while $p(\mathbf{r}_2, \dots, \mathbf{r}_J | \mathbf{r}_1)$ is the conditional probability density and can be defined as:

$$p(\mathbf{r}_2, \dots, \mathbf{r}_J | \mathbf{r}_1) := \frac{p(\mathbf{r}_1, \dots, \mathbf{r}_J)}{p(\mathbf{r}_1)}. \quad (28)$$

To calculate the ensemble average of the transmitted field, it is helpful to write the field in the following form:

$$u(\mathbf{r}) = [u_{\text{inc}}(\mathbf{r}) + u_{\text{sc}}(\mathbf{r})] \chi_{\mathcal{R} \setminus \mathcal{P}}(\mathbf{r}) + \sum_j u_{\text{in}}^j(\mathbf{r}) \chi_{\mathcal{P}_j}(\mathbf{r}), \quad (29)$$

where

$$\chi_{\mathcal{A}}(\mathbf{r}) = \begin{cases} 1 & \text{if } \mathbf{r} \in \mathcal{A}, \\ 0 & \text{if } \mathbf{r} \notin \mathcal{A}. \end{cases} \quad (30)$$

By taking the ensemble average of equation (29) we obtain:

$$\langle u(\mathbf{r}) \rangle = \langle u_{\text{inc}}(\mathbf{r}) \chi_{\mathcal{R} \setminus \mathcal{P}}(\mathbf{r}) \rangle + \langle u_{\text{sc}}(\mathbf{r}) \chi_{\mathcal{R} \setminus \mathcal{P}}(\mathbf{r}) \rangle + J \langle u_{\text{in}}^1(\mathbf{r}) \chi_{\mathcal{P}_1}(\mathbf{r}) \rangle, \quad (31)$$

where each term of the sum in (29) is the same after ensemble averaging because they are all integrated over the same domain, which means that all particles are indistinguishable from each other. To calculate (31) we need to make a few assumptions.

Isotropy and homogeneity assumption. We assume isotropy and homogeneity, which means that $p(\mathbf{r}_1)$, the probability density of one particle being at \mathbf{r}_1 , is a constant. Then, because the integral of $p(\mathbf{r}_1)$ over \mathcal{R}_1 has to equal 1, we conclude that:

$$p(\mathbf{r}_1) = \frac{1}{|\mathcal{R}_1|} = \frac{\mathbf{n}}{J}, \quad (32)$$

where $|\mathcal{R}_1|$ is the volume of \mathcal{R}_1 , J is the total number of particles, and \mathbf{n} is the number density of particles defined by:

$$\mathbf{n} := \frac{J}{|\mathcal{R}_1|} = \frac{\phi}{|\mathcal{P}_1|}, \quad (33)$$

with ϕ being the particle volume fraction, and $|\mathcal{P}_1|$ being the volume of a particle.

Isotropy and homogeneity also imply that [5] the pair-correlation g had the form (11). For convenience, we now use the form:

$$p(\mathbf{r}_2 | \mathbf{r}_1) = \frac{\mathbf{n}}{J-1} g(|\mathbf{r}_1 - \mathbf{r}_2|). \quad (34)$$

The term $(J - 1)$ appears now, rather than J , due to there being a finite number of particles, and it ensures that $g(|\mathbf{r}_1 - \mathbf{r}_2|) \rightarrow 1$ when particles become uncorrelated, as confirmed by [39, equation (8.1.2)]. For more details on the pair-correlation see [39].

Correlation distance assumption. We can only resolve the integrals appearing in equation (31) when \mathbf{r} satisfies:

$$\min_{\mathbf{r}_1 \in \partial\mathcal{R}_1} |\mathbf{r} - \mathbf{r}_1| \geq b_{12} + a, \quad (35)$$

that is, when the distance of \mathbf{r} to the boundary $\partial\mathcal{R}_1$ is greater than $b_{12} + a$. The distance b_{12} appears in (11) and is sometimes called the correlation length. Our analysis shows that when (35) is true, the transmitted field (31) is a sum of effective waves, and the incident wave is no more.

Quasi-crystalline assumption. To calculate equation (31) we assume the closure assumption known as the quasi-crystalline approximation (QCA). Details are given in [7, 8, 37].

The calculations needed to simplify the ensemble averages in (31) are shown in appendices B.1–B.3. To summarise, with all given assumptions, equation (31) leads to:

$$\langle u(\mathbf{r}) \rangle = (1 - \phi) u_{\text{inc}}(\mathbf{r}) + J \langle u_{\text{sc}}^1(\mathbf{r}) \chi_{\mathcal{R} \setminus \mathcal{P}_1}(\mathbf{r}) \rangle - J(J-1) \langle u_{\text{sc}}^1(\mathbf{r}) \chi_{\mathcal{P}_2}(\mathbf{r}) \rangle + J \langle u_{\text{in}}^1(\mathbf{r}) \chi_{\mathcal{P}_1}(\mathbf{r}) \rangle, \quad (36)$$

where the terms in equation (36) are given by (B.3), equations (B.11) and (B.16). In section 4.1 we show that equation (36) is a sum of waves.

4.1. Transmitted effective waves

In this section, we use the effective wave assumption to demonstrate that (36) is composed of functions which satisfy effective wave equations. We show that:

$$\langle u(\mathbf{r}) \rangle = w_{\text{inc}}(\mathbf{r}) + \sum_{p=1}^{\infty} w_p(\mathbf{r}), \quad (37)$$

where

$$\nabla^2 w_{\text{inc}}(\mathbf{r}) + k^2 w_{\text{inc}}(\mathbf{r}) = 0 \quad \text{and} \quad \nabla^2 w_p(\mathbf{r}) + k_p^2 w_p(\mathbf{r}) = 0. \quad (38)$$

We also show that $w_{\text{inc}}(\mathbf{r}) = 0$ when (35) holds, and when using the effective boundary condition which is deduced from first principles in [7]. That is, the incident wave is not present inside the material³.

For what follows, to keep the notation concise, we define the ball region using standard set-builder notation:

$$\mathcal{B}(\mathbf{x}; R) = \{ \mathbf{y} \in \mathbb{R}^2 : |\mathbf{x} - \mathbf{y}| \leq R \}. \quad (39)$$

The first term in (36) is given by $(1 - \phi) u_{\text{inc}}(\mathbf{r})$, which clearly contributes to the term $w_{\text{inc}}(\mathbf{r})$ in equation (37), because the incident wave satisfies the Helmholtz equation (38)₁.

The second term $J \langle u_{\text{sc}}^1(\mathbf{r}) \chi_{\mathcal{R} \setminus \mathcal{P}_1}(\mathbf{r}) \rangle$ is more involved. In appendix B.3 we prove this term has the reduced form equation (B.11). To calculate this term, first we use (23) together with (27) to obtain:

$$\langle u_{\text{sc}}^1(\mathbf{r}) \rangle(\mathbf{r}_1) = \sum_n \langle f_n \rangle(\mathbf{r}_1) \mathbf{u}_n(k\mathbf{r} - k\mathbf{r}_1). \quad (40)$$

Following the method shown in [7], we use a series expansion of the form:

$$\langle f_n \rangle(\mathbf{r}_1) = \sum_p f_{p,n}(\mathbf{r}_1), \quad (41)$$

where each $f_{p,n}$ satisfies a Helmholtz equation: $\nabla^2 f_{p,n}(\mathbf{r}_1) + k_p^2 f_{p,n}(\mathbf{r}_1) = 0$, and the k_p and $f_{p,n}$ are determined from the governing equation of $\langle f_n \rangle(\mathbf{r}_1)$. In [7] it is shown how such a series solution can be used for any material region, where [32] proves that equation (41) applies to plane-waves.

³ We note that k can not equal k_p [37].

Using the effective wave series expansion (41) in equation (B.11) leads to:

$$J\langle u_{\text{sc}}^1(\mathbf{r}) \chi_{\mathcal{R} \setminus \mathcal{P}_1}(\mathbf{r}) \rangle = \mathfrak{n} \sum_{np} \int_{\mathcal{R}_1 \setminus \mathcal{B}(\mathbf{r};a)} f_{p,n}(\mathbf{r}_1) \mathbf{u}_n(k\mathbf{r} - k\mathbf{r}_1) d\mathbf{r}_1. \quad (42)$$

As shown in [7, section 4], we can use Green's second identity to write:

$$\int_{\mathcal{R}_1 \setminus \mathcal{B}(\mathbf{r};a)} f_{p,n}(\mathbf{r}_1) \mathbf{u}_n(k\mathbf{r} - k\mathbf{r}_1) d\mathbf{r}_1 = \frac{\mathcal{I}_{p,n}(\mathbf{r}) - \mathcal{J}_{p,n}(\mathbf{r})}{k^2 - k_p^2}, \quad (43)$$

where

$$\mathcal{I}_{p,n}(\mathbf{r}) = \int_{\partial \mathcal{R}_1} \frac{\partial f_{p,n}(\mathbf{r}_1)}{\partial \boldsymbol{\nu}_1} \mathbf{u}_n(k\mathbf{r} - k\mathbf{r}_1) - f_{p,n}(\mathbf{r}_1) \frac{\partial \mathbf{u}_n(k\mathbf{r} - k\mathbf{r}_1)}{\partial \boldsymbol{\nu}_1} dA_1, \quad (44)$$

$$\mathcal{J}_{p,n}(\mathbf{r}) = \int_{\partial \mathcal{B}(0,a)} \frac{\partial f_{p,n}(\mathbf{r} - \mathbf{x}_1)}{\partial \boldsymbol{\nu}_1} \mathbf{u}_n(k\mathbf{x}_1) - f_{p,n}(\mathbf{r} - \mathbf{x}_1) \frac{\partial \mathbf{u}_n(k\mathbf{x}_1)}{\partial \boldsymbol{\nu}_1} dA_1, \quad (45)$$

from which we can see that:

$$\nabla^2 \mathcal{I}_{p,n}(\mathbf{r}) + k^2 \mathcal{I}_{p,n}(\mathbf{r}) = 0 \text{ and } \nabla^2 \mathcal{J}_{p,n}(\mathbf{r}) + k_p^2 \mathcal{J}_{p,n}(\mathbf{r}) = 0.$$

So, clearly, $\mathcal{I}_{p,n}(\mathbf{r})$ contributes to $w_{\text{inc}}(\mathbf{r})$, while $\mathcal{J}_{p,n}(\mathbf{r})$ contributes to $w_p(\mathbf{r})$ in (37).

The third term in (36) is given by (B.18) in appendix B.3.1, which after using equation (41) and equation (40) becomes:

$$\begin{aligned} J(J-1) \langle u_{\text{sc}}^1(\mathbf{r}) \chi_{\mathcal{P}_2}(\mathbf{r}) \rangle &= \phi \mathfrak{n} \sum_{np} \int_{\mathcal{R}_1 \setminus \mathcal{B}(\mathbf{r};b_{12}-a)} f_{np}(\mathbf{r}_1) \mathbf{u}_n(k\mathbf{r} - k\mathbf{r}_1) d\mathbf{r}_1 \\ &\quad - \mathfrak{n}^2 \sum_{np} \int_{\mathcal{B}(0;b_{12}+a) \setminus \mathcal{B}(0;a_{12}-a)} f_{p,n}(\mathbf{r} - \mathbf{x}_1) \mathbf{u}_n(k\mathbf{x}_1) G(\mathbf{x}_1) d\mathbf{x}_1, \end{aligned} \quad (46)$$

where $G(\mathbf{x}_1)$ is defined in (B.20) although it is not required for our goals here.

The first integral in equation (46) is analogous to (43), so leads to terms of the form (37). The second of these integrals only has \mathbf{r} dependence in $f_{p,n}(\mathbf{r} - \mathbf{x}_1)$, and therefore contributes to $w_p(\mathbf{r})$ in equation (37).

The fourth term in (36) is given by (B.3), which after using (24), equation (41) and the change of variables from \mathbf{r}_1 to $\mathbf{x}_1 = \mathbf{r} - \mathbf{r}_1$ becomes:

$$J\langle u_{\text{in}}^1(\mathbf{r}) \chi_{\mathcal{P}_1}(\mathbf{r}) \rangle = \mathfrak{n} \sum_{pn} b_n \int_{\mathcal{B}(0;a)} f_{p,n}(\mathbf{r} - \mathbf{x}_1) \mathbf{v}_n(k_o \mathbf{x}_1) d\mathbf{r}_1, \quad (47)$$

which can only contribute to terms of the form $w_p(\mathbf{r})$ in equation (37).

4.2. The average of the incident field

In the previous section we demonstrated that (31) is a sum of terms which satisfy the background and effective wave equations as shown in equation (37). The term w_{inc} , that satisfies the background wave equation, can be seen as what remains of the incident field. In much of the literature [6, 16, 20, 22, 39] it is simply assumed that $w_{\text{inc}} := 0$. This is often called the ‘extinction theorem’, despite it being an assumption. In papers such as [24] that calculate the average field from first principals, it is not clear that $w_{\text{inc}} = 0$. Here we remove any doubt by proving that when sufficiently inside the material, given by condition (35), we have that $w_{\text{inc}} := 0$ for any incident field, any material region \mathcal{R} , any frequency, and all types of particles.

Using the results from section 4.1, we collect the terms in equation (36) that satisfy the background wave equation to obtain:

$$w_{\text{inc}}(\mathbf{r}) = (1 - \phi) u_{\text{inc}}(\mathbf{r}) + \sum_{pn} \frac{\mathfrak{n}(1 - \phi)}{k^2 - k_p^2} \mathcal{I}_{p,n}(\mathbf{r}). \quad (48)$$

Here we show that the right side of equation (48) is zero by using the ensemble boundary condition given by [7, equation (4.8)]:

$$\sum_{n'} \mathcal{V}_{n'n}(k\mathbf{r}_1) g_{n'} + \mathfrak{n} \sum_{nn'p} \frac{\mathcal{I}_{p,n'n}(\mathbf{r}_1)}{k^2 - k_p^2} = 0, \quad (49)$$

where

$$\mathcal{I}_{p,n'n}(\mathbf{r}_1) = \int_{\partial\mathcal{R}_1} \mathcal{U}_{n'n}(k\mathbf{r}_1 - k\mathbf{r}_2) \frac{\partial f_{p,n'}(\mathbf{r}_2)}{\partial \nu_2} - \frac{\partial \mathcal{U}_{n'n}(k\mathbf{r}_1 - k\mathbf{r}_2)}{\partial \nu_2} f_{p,n'}(\mathbf{r}_2) dA_2, \quad (50)$$

with \mathbf{r}_2 being the variable of integration and ν_2 the normal to the boundary $\partial\mathcal{R}_1$, and the g_n are the coefficients of the incident wave:

$$u_{\text{inc}}(\mathbf{r}) = \sum_n g_n v_n(k\mathbf{r}). \quad (51)$$

Equation (51) assumes the source of the incident wave is outside of the region where the particles are [7]. The other assumptions needed to deduce the ensemble boundary conditions equation (49) are the same assumptions we have used for the calculations in this paper, except the boundary condition is only valid when:

$$\min_{\mathbf{r}_2 \in \partial\mathcal{R}_1} |\mathbf{r}_1 - \mathbf{r}_2| \geq a_{12}. \quad (52)$$

To start the demonstration, we multiply both sides of equation (49) by $v_n(k\mathbf{r} - k\mathbf{r}_1)$ and sum over n to obtain:

$$\sum_{nn'} \mathcal{V}_{n'n}(k\mathbf{r}_1) g_{n'} v_n(k\mathbf{r} - k\mathbf{r}_1) + n \sum_{nn'p} \frac{\mathcal{I}_{p,n'n}(\mathbf{r}_1)}{k^2 - k_p^2} v_n(k\mathbf{r} - k\mathbf{r}_1) = 0. \quad (53)$$

Now, equation (53) can be simplified by using the fundamental property of translation matrices that:

$$\begin{cases} v_n(k\mathbf{r} + k\mathbf{d}) = \sum_{n'} \mathcal{V}_{nn'}(k\mathbf{d}) v_{n'}(k\mathbf{r}), & \text{for all } \mathbf{d} \\ u_n(k\mathbf{r} + k\mathbf{d}) = \sum_{n'} \mathcal{U}_{nn'}(k\mathbf{d}) v_{n'}(k\mathbf{r}), & |\mathbf{r}| < |\mathbf{d}| \end{cases}. \quad (54)$$

Using the property of the translation matrices (54) together with equation (51), we see that:

$$\sum_{nn'} \mathcal{V}_{n'n}(k\mathbf{r}_1) g_{n'} v_n(k\mathbf{r} - k\mathbf{r}_1) = \sum_n g_n v_n(k\mathbf{r}) = u_{\text{inc}}(\mathbf{r}), \quad (55)$$

in accordance with [7, equation (2.3)].

Next, by choosing \mathbf{r} such that (35) is satisfied, it is then possible to choose \mathbf{r}_1 so that the condition (52) is true and such that:

$$|\mathbf{r} - \mathbf{r}_1| < |\mathbf{r}_1 - \mathbf{r}_2| \quad \text{for every } \mathbf{r}_2 \in \partial\mathcal{R}_1.$$

This enables us to use the translation property equation (54) in (50) to obtain:

$$\begin{aligned} & \sum_n \mathcal{I}_{p,n'n}(\mathbf{r}_1) v_n(k\mathbf{r} - k\mathbf{r}_1) \\ &= \int_{\partial\mathcal{R}_1} \sum_n v_n(k\mathbf{r} - k\mathbf{r}_1) \mathcal{U}_{n'n}(k\mathbf{r}_1 - k\mathbf{r}_2) \frac{\partial f_{p,n'}(\mathbf{r}_2)}{\partial \nu_2} - \sum_n v_n(k\mathbf{r} - k\mathbf{r}_1) \frac{\partial \mathcal{U}_{n'n}(k\mathbf{r}_1 - k\mathbf{r}_2)}{\partial \nu_2} f_{p,n'}(\mathbf{r}_2) dA_2 \\ &= \int_{\partial\mathcal{R}_1} u_{n'}(k\mathbf{r} - k\mathbf{r}_2) \frac{\partial f_{p,n'}(\mathbf{r}_2)}{\partial \nu_2} - \frac{\partial u_{n'}(k\mathbf{r} - k\mathbf{r}_2)}{\partial \nu_2} f_{p,n'}(\mathbf{r}_2) dA_2 = \mathcal{I}_{p,n'}(\mathbf{r}). \end{aligned} \quad (56)$$

Substituting (55) and equation (56) into equation (53) leads to:

$$u_{\text{inc}}(\mathbf{r}) + n \sum_{n'p} \frac{\mathcal{I}_{p,n'}(\mathbf{r})}{k^2 - k_p^2} = 0. \quad (57)$$

Finally, substituting (57) into (48), we conclude the extinction theorem $w_{\text{inc}}(\mathbf{r}) = 0$ for \mathbf{r} that satisfies (35). That is, there is no term in the average transmitted wave that satisfies the background wave equation.

5. Conclusions

The initial goal of this work was to find clear evidence that there exist at least two effective wavenumbers in an averaged particulate material. It is highly unusual to have two different wavenumbers for an isotropic homogeneous media supporting only scalar waves. However theoretical works [7, 19, 30, 32, 46, 47] have predicted the existence of at least two effective wavenumbers, and their presence changes the overall transmitted and reflected waves.

Monte Carlo results. To verify the existence of multiple effective wavenumbers we used very precise simulations that calculated scattered waves from different particle configurations and then took an average over the different particle configurations. This turned out to be far more computationally intensive than we expected, and required extensive and careful analysis. To summarise, figure 8 clearly shows that there are two separate wavenumbers that contribute to the field, and that the wavenumbers predicted by the Monte-Carlo method are similar to the wavenumbers predicted by the theory.

When it matters. A natural question that appeared during this work was how to find the parameters that led to multiple effective wavenumbers. That is, for what scenarios will the classical theory that uses only one effective wavenumber [2, 6, 14, 18, 24, 48] be inaccurate? Previous work [7, 30] demonstrated that there is a dispersion equation (13) which provides the effective wavenumbers k_p , and that if there is only one wavenumber k_1 with an imaginary part much smaller than all others $\text{Im } k_1 \ll \text{Im } k_p$ for $p = 2, \dots$, then the classical theory will be accurate.

However, solving the dispersion equation (13) can be time-consuming, especially for higher frequencies and a wide range of parameters. When plotting the regions where multiple wavenumbers appear we saw a clear pattern shown in figure 1: particles which are strong scatterers lead to multiple effective wavenumbers. In figure 1 the green curves show the scattering strength of just one particle equation (18). Finding the parameters that lead one particle to be a strong scatterer is far more practical than solving the dispersion equation (13), and proved to be a surprisingly good measure. To summarise: strong multiple scattering triggers multiple effective wavenumbers.

Resonators. In the field of metamaterials, strong scatterers such as resonators are often used to tailor the overall behaviour of the material [49]. Using this strategy for disordered, or random, particulates will lead to multiple effective wavenumbers, and will complicate how to predict the overall properties of the material. To truly understand the effect of these resonators it is first necessary to plot their dispersion diagrams by solving the dispersion equation (13) with the T -matrix T_n depending on the type of particle used. An example of such a diagram is given in figure 5.

Further applications. Whether we use acoustic, electromagnetic or elastic waves, the mathematical framework introduced in this paper contributes to the understanding of how the average wave will behave as it interacts with particulates within a medium. Examples of applications in the fields of telecommunications, medical and ultrasonic imaging, and optical filters can be found in [50–54].

The theoretical results. When deciding how best to sample the transmitted field, we realised that within the theoretical formulation for ensemble averaging particulates, it was not clear that the transmitted wave is a sum of waves with effective wavenumbers. This led us to derive the missing results and provide a general proof about the incident and transmitted waves.

Proof of extinction. It is often assumed that the average field inside a random material does not contain any remnant of the incident wave. This is called the Ewald–Oseen extinction theorem, but as far as the authors are aware, there is no proof of this conjecture for particulate materials. In this work, we were able to prove this extinction theorem for any particulate (for scalar isotropic waves), any frequency, and material geometry. The proof is given in section 4, with the final equation that proves extinction being equation (57). The proof also provides the extinction length: the distance required for the incident wave to travel with the material until it is extinct. We proved that the extinction length is equal to the correlation length plus the particle radius $b_{12} + a$, see equation (11) where these quantities are relative to the pair-correlation.

Proof of transmitted effective waves. The same proof for extinction also served to prove that the average transmitted field is a sum of effective waves, when the distance from the material boundary is greater than the extinction length. The proof is shown in section 4. We note, that particularly in the field of continuously varying random media [6, 55], it is assumed that the average transmitted field satisfies an effective wave

equation. By proving this for particulates, from a microscopic approach, we provide a link between the two approaches.

Future avenues. This work shows that using Monte-Carlo simulations to approximate a semi-infinite media, such as a plate, filled with particles, is still computationally challenging. We feel that future work focused on validating effective theories for particulates should focus on finite materials (in the computational sense), such as a cylinder filled with cylindrical particles and a sphere filled with spherical particles. There is a theoretical framework to validate against [7]. In terms of theoretical developments, our work has shown a connection between the particulate microscopic approach to effective waves [2, 3, 7, 16, 23] and approaches for continuously varying random media [6, 55]. That is, we demonstrate the effective wave series used in the macroscopic approach given by equation (41) does lead to the average transmitted wave being a sum of effective waves, as illustrated by equation (37). We believe the calculations we provide now pave the way to answer the following open question: are the two approaches equivalent?

Data availability statement

The data that support the findings of this study are openly available at the following URL/DOI: <http://doi.org/10.5281/zenodo.8252818>.

Acknowledgments

The authors would like to acknowledge Kevish Napal for insightful and helpful discussions. Aristeidis Karnezis gratefully acknowledges travel support from the UK Acoustics Network (EP/V007866/1, EP/R005001/1). Artur Gower gratefully acknowledges support from EPSRC (EP/V012436/1). Paulo Piva gratefully acknowledges funding from an EPSRC Case studentship with Johnson Matthey.

Author contributions

A K conceived of the study, drafted the manuscript, wrote all the code for the numerical calculations, developed the theoretical calculations, and produced all the figures. A L G helped conceive the study, edited the manuscript, assisted with and verified the theoretical calculations. P S P assisted with the projection method and with the figures related to this method, verified the calculations, and edited the manuscript.

Data and reproducibility

To produce our results we used the open source software [56–58].

Appendix A. The Monte-Carlo methodology

Here we present more details on how we performed the Monte-Carlo simulations, and analysed the results. For a reference on Monte-Carlo methods we refer to the book [39].

To compute the ensemble average wave equation (9) with Monte-Carlo simulations, the waves scattered by particles within a plate geometry (as shown in figure 2) have to be simulated tens of thousands of times, with each simulation having hundreds of particles, before the standard error of the mean converges [15]. For each simulation we calculate exactly how the incident wave $u_{\text{inc}}(x) = e^{ikx}$ scatters from all the particles using [56]. Other more sophisticated methods exist such as [59, 60], which divide the particles into rows, and calculate the transmission and reflection between these rows. These methods can be efficient and also give insight into the wave directionality. For these reasons, careful considerations are needed to determine how to perform the Monte-Carlo simulations.

In order, we explain how we created each particle configuration, how we determined the plate width and height, including consideration of convergence, and finally, how we analysed the data.

Sequential addition. To place the particles we use the strategy of Sequential addition as described in chapter 8, section 2 of [39]. In essence, we place one particle at a time according to a random uniform distribution. If the particle overlaps with another particle it is rejected. The process is repeated until we obtain a desired particle volume fraction ϕ .

The plate width. Choosing an appropriate width W for the plate \mathcal{R} was based on two factors:

- The result from the theory shown by equation (12) predicts the plate needs to have a width $W > 2a + 2b_{12}$ for $\langle u(x) \rangle$ to be exactly equal to a sum of effective waves. The minimum value for b_{12} is a_{12} , which we found to be accurate enough for our tolerances. Using $b_{12} = a_{12} > 2a$ implies that we need a plate with $W > 6a = 7.2$, as we used $a = 1.2$ for all numerical experiments.
- The plate width W can not be too wide, otherwise the average wave $\langle u(x) \rangle$ will be completely attenuated, which is a computational waste. Also, in the region where the wave is completely attenuated it is impossible to estimate the k_p by fitting equation (12). Materials, and frequencies, that lead to equation (12) needing more than one effective wavenumber k_1 to accurately approximate $\langle u(x) \rangle$ are highly attenuating materials. See figure 7 for an illustration of the region where we fit equation (12).

The plate height. If the plate filled with particles, as shown in figure 2, was infinite in height, and the particles were excited by a plane-wave, then the average wave $\langle u(x) \rangle$ would be exactly a sum of plane-waves given by equation (12). See [7] for details. In practice, it is not of course possible to exactly simulate the wave scattered from an infinite plate filled with one specific arrangement of particles. The approximation often used is to have a cell filled with a random set of particles, and then to use periodic tilling of this cell [28]. To avoid the artifacts produced by periodic tilling we perform a convergence study to determine at what height a plate filled with particles behaves approximately like a plate of infinite size.

Let H be the height of the plate, which is illustrated in figure 2. To determine the size needed for H , we first choose a large value $H = 600$, with the plate width $W = 20$, and then filled this plate with one configuration of particles Λ , according to the sequential addition method. We then calculate the total wave at:

$$u(x, 0) \quad \text{for the values } 2a \leq x \leq W - 2a, \quad (\text{A.1})$$

to create a function $\mathbf{U}_{600}(x)$.

To determine the influence of H , we then reduce the height. For example, we use $H = 590$ and remove from Λ any particles that are now outside of the box with the reduced height. We then take the updated configuration of particles Λ and recalculate the total wave in the same region to create the function $\mathbf{U}_{590}(x)$.

For a range of heights we compute the relative error:

$$\text{Error \%} = 100 \frac{\|\mathbf{U}_H(x) - \mathbf{U}_{600}(x)\|}{\|\mathbf{U}_{600}(x)\|}. \quad (\text{A.2})$$

By calculating these errors for a range of heights we can plot the error against the height as shown in figure A1.

For sound-soft particles, see table 1 for details, and frequency $ka = 0.3$, we see that the errors have converged. This means that $\mathbf{U}_{600}(x)$ is approximately the same as $\mathbf{U}_\infty(x)$, and we can estimate that the height of the plate has to be approximately $H = 400$ for the scattered waves to have an error of less than 1% in comparison to $\mathbf{U}_\infty(x)$.

For sound-hard particles, see table 1 for details, and $ka = 0.3$, the errors have not converged as can be seen from figure A1, even for very larger heights. This means it is unclear what is the error relative to an infinite plate \mathbf{U}_∞ . For this reason, we do not focus on this case, and only performed one simulation with $H = 400$. Our hypothesis is that the plane-wave when scattered from the corner of the plate leads to a transmitted wave that travels down inside the plate relatively unobstructed, as these types of particles are weak scatterers.

When fitting for the effective wavenumbers, we need to consider how the errors due to truncating the height of the plate may affect the fitting and the acceptable fitting errors.

Analysing the data. We generate Monte-Carlo simulations for the different cases presented in section 3.1 with a plate of width $W = 20$ and height $H = 400$. The data from Monte-Carlo results for the transmitted wave equation (12) is of the form:

$$\langle u(x, 0; \Lambda) \rangle = \sum_{p=1}^P (A_p^+ e^{ik_p x} + A_p^- e^{-ik_p x}) + \epsilon(x), \quad \text{for } 2a \leq x \leq W - 2a, \quad (\text{A.3})$$

where $\epsilon(x)$ is a small error that falls inside the standard error of the mean. For the cases where only one effective wavenumber was predicted, the average wave $\langle u(x, 0; \Lambda) \rangle$ is fitted well by equation (1), using non-linear optimisation libraries in Julia [58].

For every wavenumber k_p there are potentially two waves: one travelling towards the positive x -direction and another travelling in the negative x -direction. For the cases where the average wave is completely

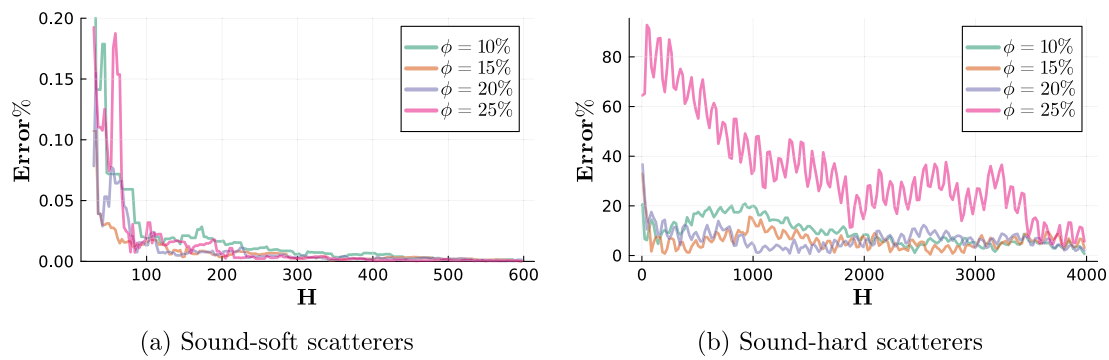


Figure A1. Shows the rate of convergence which can be described with the normalised difference between the scattered waves equation (A.2) with respect to the height of the plate H .

attenuated when it reaches the edge of the plate, $x = 20$, we should have $A_p^- = 0$, suppressing the wave travelling in the negative x -direction.

From the Monte-Carlo data for cases with more than one effective wavenumber, we find that $\langle u(x, 0; \Lambda) \rangle$ is below the standard error of the mean for $x \geq 15$. For this reason, we can take $A_p^- = 0$ and fit only for A_p^+ and k_p . That is we fit to the Monte-Carlo data functions of the form:

$$h(x) = \sum_{p=1}^P A_p^+ e^{ik_p x}, \quad \text{for } 4 \leq x \leq 15, \quad (\text{A.4})$$

with $\text{Im}[k_p] > 0$. In the case presented in figure 7(a) the transmitted wave attenuates quicker, therefore we focus the fitting on a narrower range, $4 \leq x \leq 10$.

Another reason to use equation (A.4), is that fitting for A_p^+ , A_p^- , and k_p in the case of multiple effective wavenumbers can become ill-posed. This is related to how inverting a Laplace transform is ill-posed, see section 2.1 of [61]. That is, the more terms included in the sum shown in equation (12) the more ill-posed is the problem of recovering the k_p , A_p^+ , and A_p^- from data of the average wave $\langle u(x, 0; \Lambda) \rangle$.

For the cases with more than one effective wavenumber, non-linear optimisation [58] is unstable. Therefore, we implement a method, the *Projection method*, to both fit equation (A.4) and estimate the sensitivity of the parameters k_p to the data.

Projection Method. To fit Monte-Carlo data for the cases with more than one effective wavenumbers, we design an algorithm that sweeps over all possible values of the wavenumbers k_p and for each case performs a linear fit, by using least-squares, to predict the amplitudes A_p^+ in equation (A.4). For that, we consider a mesh in the complex plane $\mathcal{C} \subset \mathbb{C}$ from which we sample values of k_p . A sketch of the algorithm for the case $P = 3$ is given in algorithm 1.

Algorithm 1. Algorithm for the projection method.

```

Data:  $\langle u(x, 0; \Lambda) \rangle$ 
for all values of  $k_1 \in \mathcal{C}$  do
  for all values of  $k_2, k_3 \in \mathcal{C}$  do
    if  $k_1 \neq k_2 \neq k_3$  then
      Determine the values of  $A_p^+$  that best fit  $\langle u(x, 0; \Lambda) \rangle$  using
      least-squares ;
      Using equation (A.4), compute the error
       $\varepsilon(k_1, k_2, k_3) = \|h(x) - \langle u(x, 0; \Lambda) \rangle\|$  ;
      Store  $\varepsilon(k_1, k_2, k_3)$ ;
    end
  end
  Store  $\varepsilon(k_1) = \min_{k_2, k_3} \varepsilon(k_1, k_2, k_3)$ 
end
Result:  $\varepsilon(k_1)$ 

```

The algorithm calculates the minimum error $\varepsilon(k_1)$ for every possible k_1 , and it is this error which is shown in figures 8 and 9(b), (d). We perform further analysis to establish if the optimal wavenumbers are

located at the local minima shown, and whether the fitted curves when using equation (A.4) are within the standard error of the mean of the Monte-Carlo simulation. The blue region in figure 8, contains all wavenumbers for which the fitted curves are within the standard error of the mean. There are clearly two distinct disconnected regions for possible values of k_p , which shows that the transmitted wave is composed of a sum of two effective waves.

Computational time. Our study utilises high-fidelity Monte-Carlo simulations, whose computational cost was significant. This limits the number of cases we could investigate with Monte-Carlo. For example, we needed to execute 40 000 simulations for scenarios depicted in figures 7–9. Each simulation involves hundreds of particles, and is computationally demanding especially at higher frequencies denoted by ka . To manage this, we employed parallel processing across multiple processors. For instance, simulating sound-soft particles at a frequency of $ka = 0.36$ requires about 72h for completion on an 11th Gen. Intel Core i7 with 8 cores. So without parallel processing, the runtime would increase by at least eight-fold.

Appendix B. The ensemble average transmission

Here we reduce the terms in (31) to reach equation (36). For this section we use the notation and assumptions introduced in section 4.

In many calculations throughout this section, for any function f which depends on particle configuration, we use that:

$$J\langle f \rangle = J \int_{\mathcal{R}_1^J} f p(\mathbf{r}_1, \dots, \mathbf{r}_J) d\mathbf{r}_1 \cdots d\mathbf{r}_J \quad (\text{B.1})$$

$$= n \int_{\mathcal{R}_1^J} f p(\mathbf{r}_2, \dots, \mathbf{r}_J | \mathbf{r}_1) d\mathbf{r}_1 \cdots d\mathbf{r}_J = n \int_{\mathcal{R}_1} \langle f \rangle(\mathbf{r}_1) d\mathbf{r}_1, \quad (\text{B.2})$$

where we used, in order, the definitions equations (26), (28) and (32). If the f only depends on \mathbf{r}_1 , then we further have that $\langle f \rangle(\mathbf{r}_1) = f$ because:

$$\int_{\mathcal{R}_1^{J-1}} p(\mathbf{r}_2, \dots, \mathbf{r}_J | \mathbf{r}_1) d\mathbf{r}_2 \cdots d\mathbf{r}_J = 1,$$

which is true for any joint probability density.

B.1. The transmitted internal field

We start by calculating the simplest term. Using equation (24), the definitions of the ensemble average equations (27) and (26), then equation (B.1) leads to:

$$J\langle u_{\text{in}}^1(\mathbf{r}) \chi_{\mathcal{P}_1}(\mathbf{r}) \rangle = n \int_{\mathcal{B}(\mathbf{r}; a)} \langle u_{\text{in}}^1(\mathbf{r}) \rangle(\mathbf{r}_1) d\mathbf{r}_1, \quad (\text{B.3})$$

where the ball $\mathcal{B}(\mathbf{r}; a)$ is defined by equation (39), and we use the assumption (35).

B.2. The transmitted incident field

The next simplest computation is the ensemble average of the incident wave term in (31). To do this we will demonstrate the following equalities:

$$\langle u_{\text{inc}}(\mathbf{r}) \chi_{\mathcal{R} \setminus \mathcal{P}}(\mathbf{r}) \rangle = u_{\text{inc}}(\mathbf{r}) \langle \chi_{\mathcal{R} \setminus \mathcal{P}}(\mathbf{r}) \rangle = u_{\text{inc}}(\mathbf{r}) \langle 1 - \chi_{\mathcal{P}}(\mathbf{r}) \rangle = u_{\text{inc}}(\mathbf{r}) (1 - \phi), \quad (\text{B.4})$$

where ϕ is the particle volume fraction defined by (33).

First, we use the ensemble average (26), then take $u_{\text{inc}}(\mathbf{r})$ outside of the integrals, as it does not depend on the particle positions, to reach:

$$\langle u_{\text{inc}}(\mathbf{r}) \chi_{\mathcal{R} \setminus \mathcal{P}}(\mathbf{r}) \rangle = u_{\text{inc}}(\mathbf{r}) \langle \chi_{\mathcal{R} \setminus \mathcal{P}}(\mathbf{r}) \rangle. \quad (\text{B.5})$$

To calculate the ensemble average on the right we use:

$$\chi_{\mathcal{R} \setminus \mathcal{P}}(\mathbf{r}) = 1 - \chi_{\mathcal{P}}(\mathbf{r}), \quad (\text{B.6})$$

leading to:

$$\langle \chi_{\mathcal{R} \setminus \mathcal{P}}(\mathbf{r}) \rangle = \langle 1 \rangle - \langle \chi_{\mathcal{P}}(\mathbf{r}) \rangle = 1 - \sum_j \langle \chi_{\mathcal{P}_j}(\mathbf{r}) \rangle, \quad (\text{B.7})$$

where we used the definition that integrating a probability density function p over all its variables gives 1, and:

$$\chi_{\mathcal{P}}(\mathbf{r}) p(\mathbf{r}_1, \mathbf{r}_2, \dots, \mathbf{r}_J) = \sum_{j=1}^J \chi_{\mathcal{P}_j}(\mathbf{r}) p(\mathbf{r}_1, \mathbf{r}_2, \dots, \mathbf{r}_J), \quad (\text{B.8})$$

which holds because if any two particles overlap, we have that $p(\mathbf{r}_1, \mathbf{r}_2, \dots, \mathbf{r}_J) = 0$. Therefore, if $\chi_{\mathcal{P}_j}(\mathbf{r}) = 1$, then $\chi_{\mathcal{P}_\ell}(\mathbf{r}) = 0$ for $\ell \neq j$.

Next, we use that particles are indistinguishable, except for their positions, so after ensemble averaging $\langle \chi_{\mathcal{P}_j}(\mathbf{r}) \rangle = \langle \chi_{\mathcal{P}_1}(\mathbf{r}) \rangle$ for every j , which together with equation (B.1) leads to:

$$\langle \chi_{\mathcal{P}}(\mathbf{r}) \rangle = \sum_{j=1}^J \langle \chi_{\mathcal{P}_j}(\mathbf{r}) \rangle = J \langle \chi_{\mathcal{P}_1}(\mathbf{r}) \rangle = n \int_{\mathcal{R}_1} \chi_{\mathcal{P}_1}(\mathbf{r}) d\mathbf{r}_1 = n \int_{\mathcal{B}(\mathbf{r}, a)} d\mathbf{r}_1 = \phi, \quad (\text{B.9})$$

where we used (35) and (39).

B.3. The transmitted scattered field

The most involved term to calculate in equation (31) is $\langle u_{\text{sc}}(\mathbf{r}) \chi_{\mathcal{R} \setminus \mathcal{P}}(\mathbf{r}) \rangle$, which will require that we demonstrate the following steps:

$$\begin{aligned} \langle u_{\text{sc}}(\mathbf{r}) \chi_{\mathcal{R} \setminus \mathcal{P}}(\mathbf{r}) \rangle &= \sum_j \langle u_{\text{sc}}^j(\mathbf{r}) \chi_{\mathcal{R} \setminus \mathcal{P}}(\mathbf{r}) \rangle = J \langle u_{\text{sc}}^1(\mathbf{r}) \chi_{\mathcal{R} \setminus \mathcal{P}}(\mathbf{r}) \rangle = J \langle u_{\text{sc}}^1(\mathbf{r}) \prod_{j=1}^J \chi_{\mathcal{R} \setminus \mathcal{P}_j}(\mathbf{r}) \rangle \\ &= J \langle u_{\text{sc}}^1(\mathbf{r}) \chi_{\mathcal{R} \setminus \mathcal{P}_1}(\mathbf{r}) \rangle - J \sum_{j=2}^J \langle u_{\text{sc}}^1(\mathbf{r}) \chi_{\mathcal{P}_j}(\mathbf{r}) \rangle \\ &= J \langle u_{\text{sc}}^1(\mathbf{r}) \chi_{\mathcal{R} \setminus \mathcal{P}_1}(\mathbf{r}) \rangle - J(J-1) \langle u_{\text{sc}}^1(\mathbf{r}) \chi_{\mathcal{P}_2}(\mathbf{r}) \rangle. \end{aligned} \quad (\text{B.10})$$

The first three equalities in equation (B.10) are a result of using, in order, equation (23), that particles are indistinguishable, and:

$$\chi_{\mathcal{R} \setminus \mathcal{P}}(\mathbf{r}) p(\mathbf{r}_1, \mathbf{r}_2, \dots, \mathbf{r}_J) = \prod_{j=1}^J \chi_{\mathcal{R} \setminus \mathcal{P}_j}(\mathbf{r}) p(\mathbf{r}_1, \mathbf{r}_2, \dots, \mathbf{r}_J),$$

which is a result of $p(\mathbf{r}_1, \mathbf{r}_2, \dots, \mathbf{r}_J) = 0$ when any two particles overlap. The non-overlapping of particles also leads to:

$$\chi_{\mathcal{R} \setminus \mathcal{P}_1}(\mathbf{r}) \prod_{j=2}^J \chi_{\mathcal{R} \setminus \mathcal{P}_j}(\mathbf{r}) p(\mathbf{r}_1, \mathbf{r}_2, \dots, \mathbf{r}_J) = \left[\chi_{\mathcal{R} \setminus \mathcal{P}_1}(\mathbf{r}) - \sum_{j=2}^J \chi_{\mathcal{P}_j}(\mathbf{r}) \right] p(\mathbf{r}_1, \mathbf{r}_2, \dots, \mathbf{r}_J),$$

which we use to conclude the second line in equation (B.10), and the third line is just a result of particles being indistinguishable again.

We proceed by simplifying the last two terms in (B.10). Using equation (B.1) we can reach:

$$J \langle u_{\text{sc}}^1(\mathbf{r}) \chi_{\mathcal{R} \setminus \mathcal{P}_1}(\mathbf{r}) \rangle = n \int_{\mathcal{R}_1} \langle u_{\text{sc}}^1(\mathbf{r}) \rangle(\mathbf{r}_1) \chi_{\mathcal{R} \setminus \mathcal{P}_1}(\mathbf{r}) d\mathbf{r}_1 = n \int_{\mathcal{R}_1 \setminus \mathcal{B}(\mathbf{r}, a)} \langle u_{\text{sc}}^1(\mathbf{r}) \rangle(\mathbf{r}_1) d\mathbf{r}_1, \quad (\text{B.11})$$

where $\langle u_{\text{sc}}^1(\mathbf{r}) \rangle(\mathbf{r}_1)$ is given by (40).

For the last term in (B.10), we further use:

$$p(\mathbf{r}_2, \dots, \mathbf{r}_J | \mathbf{r}_1) = p(\mathbf{r}_2 | \mathbf{r}_1) p(\mathbf{r}_3, \dots, \mathbf{r}_J | \mathbf{r}_1, \mathbf{r}_2),$$

(23), equation (27), and the definition of $\langle f_n \rangle(\mathbf{r}_1, \mathbf{r}_2)$ given by [7, equations (3.10) and (3.11)], followed by analogous steps shown in equation (40), to obtain:

$$J \langle u_{\text{sc}}^1(\mathbf{r}) \chi_{\mathcal{P}_2}(\mathbf{r}) \rangle = n \sum_n \int_{\mathcal{R}_1^2} \langle f_n \rangle(\mathbf{r}_1, \mathbf{r}_2) u_n(k\mathbf{r} - k\mathbf{r}_1) p(\mathbf{r}_2 | \mathbf{r}_1) \chi_{\mathcal{P}_2}(\mathbf{r}) d\mathbf{r}_1 d\mathbf{r}_2. \quad (\text{B.12})$$

To simplify equation (B.12) we first use the QCA equation (B.13):

$$\langle f_n \rangle (\mathbf{r}_1, \mathbf{r}_2) \approx \langle f_n \rangle (\mathbf{r}_1), \quad (\text{B.13})$$

which is needed to deduce effective wavenumbers [7, 8, 14].

Before we show how to simplify equation (B.12) for a general pair-correlation g , which we show in appendix B.3.1, we first deduce the results for the simplest pair-correlation called Hole-Correction. It is far easier to understand this case first. The Hole-Correction approximation is the result of taking $b_{12} = a_{12}$ in the general pair-correlation equation (11).

Using equations (B.13) and (34) in the integral (B.12), and swapping the order of integration leads to:

$$J(J-1) \langle u_{\text{sc}}^1(\mathbf{r}) \chi_{\mathcal{P}_2}(\mathbf{r}) \rangle = n^2 \int_{\mathcal{R}_1} \langle u_{\text{sc}}^1(\mathbf{r}) \rangle (\mathbf{r}_1) \int_{\mathcal{R}_1} \chi_{\mathcal{P}_2}(\mathbf{r}) g(|\mathbf{r}_1 - \mathbf{r}_2|) d\mathbf{r}_2 d\mathbf{r}_1. \quad (\text{B.14})$$

Next we use $b_{12} = a_{12}$ and (11) which implies that:

$$g(|\mathbf{r}_1 - \mathbf{r}_2|) = \chi_{\mathcal{R}_1 \setminus \mathcal{B}(\mathbf{r}_1; a_{12})}(\mathbf{r}_2),$$

which we substitute into equation (B.14) to reach:

$$J(J-1) \langle u_{\text{sc}}^1(\mathbf{r}) \chi_{\mathcal{P}_2}(\mathbf{r}) \rangle = n^2 \int_{\mathcal{R}_1} \langle u_{\text{sc}}^1(\mathbf{r}) \rangle (\mathbf{r}_1) \int_{\mathcal{B}(\mathbf{r}; a) \setminus \mathcal{B}(\mathbf{r}_1; a_{12})} d\mathbf{r}_2 d\mathbf{r}_1, \quad (\text{B.15})$$

where we used that $\mathcal{B}(\mathbf{r}; a)$ is completely contained in \mathcal{R}_1 for every \mathbf{r}_2 due to (35). There are values for \mathbf{r}_1 for which the integral in equation (B.15) is zero. To see this we note:

$$\mathbf{r}_2 \in \mathcal{B}(\mathbf{r}; a) \implies |\mathbf{r}_2 - \mathbf{r}| \leq a \quad \text{and} \quad \mathbf{r}_2 \notin \mathcal{B}(\mathbf{r}_1; a_{12}) \implies |\mathbf{r}_2 - \mathbf{r}_1| > a_{12},$$

then from the triangular inequality we have:

$$|\mathbf{r}_1 - \mathbf{r}| \geq |\mathbf{r}_1 - \mathbf{r}_2| - |\mathbf{r}_2 - \mathbf{r}| > a_{12} - a.$$

The above implies that the region of integration for \mathbf{r}_1 is just $\mathcal{R}_1 \setminus \mathcal{B}(\mathbf{r}; a_{12} - a)$. We now further split this region of integration into two disjoint regions: the first is $\mathcal{R}_1 \setminus \mathcal{B}(\mathbf{r}; a_{12} + a)$ and the second is $\mathcal{B}(\mathbf{r}; a_{12} + a) \setminus \mathcal{B}(\mathbf{r}; a_{12} - a)$.

For the first region $\mathbf{r}_1 \in \mathcal{R}_1 \setminus \mathcal{B}(\mathbf{r}; a_{12} + a)$ implies that $|\mathbf{r}_1 - \mathbf{r}| \geq a_{12} + a$, which together with $\mathbf{r}_2 \in \mathcal{B}(\mathbf{r}; a)$ leads to:

$$|\mathbf{r}_1 - \mathbf{r}_2| \geq |\mathbf{r}_1 - \mathbf{r}| - |\mathbf{r} - \mathbf{r}_2| > a_{12},$$

due to the triangle inequality. In other words, the region of integration for \mathbf{r}_2 becomes $\mathbf{r}_2 \in \mathcal{B}(\mathbf{r}; a) \setminus \mathcal{B}(\mathbf{r}_1; a_{12}) = \mathcal{B}(\mathbf{r}; a)$.

For the second region $\mathbf{r}_1 \in \mathcal{B}(\mathbf{r}; a_{12} + a) \setminus \mathcal{B}(\mathbf{r}; a_{12} - a)$, which implies that:

$$a < a_{12} - a \leq |\mathbf{r}_1 - \mathbf{r}| \leq a_{12} + a.$$

The above guarantees that the two spheres $\mathcal{B}(\mathbf{r}; a)$ and $\mathcal{B}(\mathbf{r}_1; a_{12})$ will intersect. Let \mathcal{V} be this region of intersection, then the region of integration of \mathbf{r}_2 becomes $\mathcal{B}(\mathbf{r}; a) \setminus \mathcal{B}(\mathbf{r}_1; a_{12}) = \mathcal{B}(\mathbf{r}; a) \setminus \mathcal{V}$. This is useful as \mathcal{V} is formed of two spherical caps whose volume is easy to calculate⁴.

Using the split of these two regions for \mathbf{r}_1 we obtain:

$$\begin{aligned} J(J-1) \langle u_{\text{sc}}^1(\mathbf{r}) \chi_{\mathcal{P}_2}(\mathbf{r}) \rangle &= n^2 \int_{\mathcal{R}_1 \setminus \mathcal{B}(\mathbf{r}; a_{12} + a)} \langle u_{\text{sc}}^1(\mathbf{r}) \rangle (\mathbf{r}_1) \int_{\mathcal{B}(\mathbf{r}; a)} d\mathbf{r}_2 d\mathbf{r}_1 \\ &\quad + n^2 \int_{\mathcal{B}(\mathbf{r}; a_{12} + a) \setminus \mathcal{B}(\mathbf{r}; a_{12} - a)} \langle u_{\text{sc}}^1(\mathbf{r}) \rangle (\mathbf{r}_1) \left[\frac{4}{3} \pi a^3 - V_{\text{cap}}(|\mathbf{r} - \mathbf{r}_1|) \right] d\mathbf{r}_1 \\ &= \phi n \int_{\mathcal{R}_1 \setminus \mathcal{B}(\mathbf{r}; a_{12} - a)} \langle u_{\text{sc}}^1(\mathbf{r}) \rangle (\mathbf{r}_1) d\mathbf{r}_1 \\ &\quad - n^2 \int_{\mathcal{B}(\mathbf{r}; a_{12} + a) \setminus \mathcal{B}(\mathbf{r}; a_{12} - a)} \langle u_{\text{sc}}^1(\mathbf{r}) \rangle (\mathbf{r}_1) V_{\text{cap}}(|\mathbf{r} - \mathbf{r}_1|) d\mathbf{r}_1. \end{aligned} \quad (\text{B.16})$$

⁴ See the website <https://mathworld.wolfram.com/Sphere-SphereIntersection.html> for details.

where $V_{\text{cap}}(d)$ is the volume of \mathcal{V} and $d = |\mathbf{r} - \mathbf{r}_1|$. By using the formulas for spherical caps⁴ we can calculate that:

$$V_{\text{cap}}(d) = \frac{\pi}{12d} (a + a_{12} - d)^2 \left(d^2 + 2(a + a_{12})d - 3(a - a_{12})^2 \right).$$

B.3.1. An isotropic pair-correlation

In the previous section we chose a simple pair-correlation to simplify the integral equation (B.14). Here we show how to reduce this integral when assuming a more general form for the isotropic pair-correlation given by equation (11).

In the pair-correlation equation (11) we assume there is a value b_{12} for which $g(r) = 1$ when $r \geq b_{12}$. This is an approximation, but it is essential for the results in this section. This distance b_{12} , which is also called the correlation length, dictates at what distance inside the material the incident wave will be extinct.

Following closely the steps that led to (B.16), we now split the integral over \mathbf{r}_1 into two regions $\mathcal{R}_1 \setminus \mathcal{B}(\mathbf{r}; b_{12} + a)$ and $\mathcal{B}(\mathbf{r}; b_{12} + a) \setminus \mathcal{B}(\mathbf{r}; a_{12} - a)$, which leads to:

$$\begin{aligned} J(J-1) \langle u_{\text{sc}}^1(\mathbf{r}) \chi_{\mathcal{P}_2}(\mathbf{r}) \rangle &= n^2 \int_{\mathcal{R}_1 \setminus \mathcal{B}(\mathbf{r}; b_{12} + a)} \langle u_{\text{sc}}^1(\mathbf{r}) \rangle(\mathbf{r}_1) \int_{\mathcal{B}(\mathbf{r}; a)} d\mathbf{r}_2 d\mathbf{r}_1 \\ &\quad + n^2 \int_{\mathcal{B}(\mathbf{r}; b_{12} + a) \setminus \mathcal{B}(\mathbf{r}; a_{12} - a)} \langle u_{\text{sc}}^1(\mathbf{r}) \rangle(\mathbf{r}_1) \int_{\mathcal{B}(\mathbf{r}; a)} g(|\mathbf{r}_1 - \mathbf{r}_2|) d\mathbf{r}_2 d\mathbf{r}_1, \end{aligned} \quad (\text{B.17})$$

where we use (35) to guarantee that the ball $\mathcal{B}(\mathbf{r}; b_{12} + a)$ is completely contained within the region \mathcal{R}_1 .

Without the condition (35) it does not seem possible to show that the incident wave becomes extinct, so we hypothesize that this is a necessary condition, as well as sufficient.

The integral on the right of the first line of (B.17) was already resolved in the previous section, except now we replace a_{12} with b_{12} . For the integrals on the second line of (B.17), we use the change of variables from \mathbf{r}_2 to $\mathbf{r}_{21} = \mathbf{r}_2 - \mathbf{r}_1$ and \mathbf{r}_1 to $\mathbf{x}_1 = \mathbf{r} - \mathbf{r}_1$ to obtain:

$$J(J-1) \langle u_{\text{sc}}^1(\mathbf{r}) \chi_{\mathcal{P}_2}(\mathbf{r}) \rangle = n \phi \int_{\mathcal{R}_1 \setminus \mathcal{B}(\mathbf{r}; b_{12} + a)} \langle u_{\text{sc}}^1(\mathbf{r}) \rangle(\mathbf{r}_1) d\mathbf{r}_1 \quad (\text{B.18})$$

$$+ n^2 \int_{\mathcal{B}(\mathbf{0}; b_{12} + a) \setminus \mathcal{B}(\mathbf{0}; a_{12} - a)} \langle u_{\text{sc}}^1(\mathbf{r}) \rangle(\mathbf{r} - \mathbf{x}_1) G(\mathbf{x}_1) d\mathbf{x}_1, \quad (\text{B.19})$$

where

$$G(\mathbf{x}_1) = \int_{\mathcal{B}(\mathbf{x}_1; a)} g(r_{21}) d\mathbf{r}_{21}. \quad (\text{B.20})$$

and $r_{21} = |\mathbf{r}_{21}|$. This concludes the calculations in this section.

ORCID iDs

Aristeidis Karnezis  <https://orcid.org/0009-0002-0180-5073>

Paulo S Piva  <https://orcid.org/0000-0002-8239-970X>

Art L Gower  <https://orcid.org/0000-0002-3229-5451>

References

- [1] Ishimaru A 1978 *Wave Propagation and Scattering in Random Media: Single Scattering and Transport Theory v. 1* (Academic)
- [2] Mishchenko M I 2014 *Electromagnetic Scattering by Particles and Particle Groups: An Introduction* (Cambridge University Press)
- [3] Mishchenko M I, Travis L D and Lacis A A 2006 *Multiple Scattering of Light by Particles: Radiative Transfer and Coherent Backscattering* (Cambridge University Press)
- [4] Uscinski B J 1977 *Elements of Wave Propagation in Random Media* (McGraw-Hill)
- [5] Torquato S and Haslach H 2002 Random heterogeneous materials: microstructure and macroscopic properties *Appl. Mech. Rev.* **55** B62–B63
- [6] Carminati R and Schotland J C 2021 *Principles of Scattering and Transport of Light* (Cambridge University Press)
- [7] Gower A L and Kristensson G 2021 Effective waves for random three-dimensional particulate materials *New J. Phys.* **23** 063083
- [8] Ma Y, Varadan V V and Varadan V K 1984 Multiple scattering theory for wave propagation in discrete random media *Int. J. Eng. Sci.* **22** 1139–48
- [9] Torquato S, Zhang G and Stillinger F H 2015 Ensemble theory for stealthy hyperuniform disordered ground states *Phys. Rev. X* **5** 021020
- [10] Torquato S 2018 Hyperuniform states of matter *Phys. Rep.* **745** 1–95
- [11] Ma G and Sheng P 2016 Acoustic metamaterials: from local resonances to broad horizons *Sci. Adv.* **2** e1501595

- [12] Romero-García V, Chéron E, Kuznetsova S, Groby J P, Félix S and Pagneux V *et al* 2021 Wave transport in 1D stealthy hyperuniform phononic materials made of non-resonant and resonant scatterers *APL Mater.* **9** 10
- [13] Dubois J, Aristégui C, Ponclet O and Shuvalov A L 2011 Coherent acoustic response of a screen containing a random distribution of scatterers: comparison between different approaches *J. Phys.: Conf. Ser.* **269** 012004
- [14] Linton C M and Martin P A 2005 Multiple scattering by random configurations of circular cylinders: second-order corrections for the effective wavenumber *J. Acoust. Soc. Am.* **117** 3413
- [15] Martin P A 2006 *Multiple Scattering: Interaction of Time-Harmonic Waves With N Obstacles* (Cambridge University Press)
- [16] Tishkovets V P, Petrova E V and Mishchenko M I 2011 Scattering of electromagnetic waves by ensembles of particles and discrete random media *J. Quant. Spectrosc. Radiat. Transfer* **112** 2095–127
- [17] Tsang L, Kong J A and Habashy T 1982 Multiple scattering of acoustic waves by random distribution of discrete spherical scatterers with the quasicrystalline and Percus-Yevick approximation *J. Acoust. Soc. Am.* **71** 552–8
- [18] Varadan V K, Bringi V N, Varadan V V and Ishimaru A 1983 Multiple scattering theory for waves in discrete random media and comparison with experiments *Radio Sci.* **18** 321–7
- [19] Willis J R 2020 Transmission and reflection at the boundary of a random two-component composite *Proc. R. Soc. A* **476** 20190811
- [20] Fearn H, James D F V and Milonni P W 1996 Microscopic approach to reflection, transmission and the Ewald–Oseen extinction theorem *Am. J. Phys.* **64** 986–95
- [21] Ballenegger V C and Weber T A 1999 The Ewald–Oseen extinction theorem and extinction lengths *Am. J. Phys.* **67** 599–605
- [22] Lax M 1952 Multiple scattering of waves. II. the effective field in dense systems *Phys. Rev.* **85** 621–9
- [23] Tsang L, Kong J A and Ding K H 2000 *Scattering of Electromagnetic Waves: Theories and Applications* (Wiley)
- [24] Martin P A 2011 Multiple scattering by random configurations of circular cylinders: reflection, transmission and effective interface conditions *J. Acoust. Soc. Am.* **129** 1685–95
- [25] Muinonen K, Mishchenko M I, Dlugach J M, Zubko E, Penttilä A and Videen G 2012 Coherent backscattering verified numerically for a finite volume of spherical particles *Astrophys. J.* **760** 118
- [26] Zurk L M, Tsang L, Ding K H and Winebrenner D P 1995 Monte Carlo simulations of the extinction rate of densely packed spheres with clustered and nonclustered geometries *J. Opt. Soc. Am. A* **12** 1772
- [27] Chekroun M, Le Marrec L, Lombard B and Piraux J 2012 Time-domain numerical simulations of multiple scattering to extract elastic effective wavenumbers *Waves Random Complex Media* **22** 398–422
- [28] Chekroun M, Le Marrec L, Lombard B, Piraux J and Abraham O 2009 Comparison between a multiple scattering method and direct numerical simulations for elastic wave propagation in concrete *Ultrasonic Wave Propagation in non Homogeneous Media* (Springer) pp 317–27
- [29] Kristensson G 2023 Multiple scattering by a collection of randomly located obstacles Part V: low order contributions to the coherent fields *Technical Report LUTEDX/(TEAT-7277)/1-45/(2023)* vol TEAT-7277
- [30] Gower A L, Parnell W J and Abrahams I D 2019 Multiple waves propagate in random particulate materials *SIAM J. Appl. Math.* **79** 2569–92
- [31] Simon A, Wunnenburger R and Valier-Brasier T 2021 Propagation of coherent shear waves in scattering elastic media *Phys. Rev. E* **103** L051001
- [32] Gower A L, Abrahams I D and Parnell W J 2019 A proof that multiple waves propagate in ensemble-averaged particulate materials *Proc. R. Soc. A* **475** 20190344
- [33] Wu R S 1982 Mean field attenuation and amplitude attenuation due to wave scattering *Wave Motion* **4** 305–16
- [34] Mishchenko M I, Travis L D and Lacis A A 2002 *Scattering, Absorption and Emission of Light by Small Particles* (Cambridge University Press)
- [35] Gower A L, Hawkins S C and Kristensson G 2023 A model to validate effective waves in random particulate media: spherical symmetry *Proc. R. Soc. A* **479** 20230444
- [36] Napal K K, Piva P S and Gower A L 2023 Effective T-matrix of a cylinder filled with a random 2 dimensional particulate (arXiv:2308.13338)
- [37] Gower A L, Smith M J A, Parnell W J and Abrahams I D 2018 Reflection from a multi-species material and its transmitted effective wavenumber *Proc. R. Soc. A* **474** 20170864
- [38] Bringi V V, Varadan V and Varadan V K 1982 The effects on pair correlation function of coherent wave attenuation in discrete random media *IEEE Trans. Antennas Propag.* **30** 805–8
- [39] Tsang L, Kong J A, Ding K and Ao C O 2001 *Scattering of Electromagnetic Waves: Numerical Simulations* (Wiley)
- [40] Kristensson G, Gustavsson M and Wellander N 2021 Multiple scattering by a collection of randomly located obstacles part IV: the effect of the pair correlation function *Technical Report LUTEDX/(TEAT-7272)/1-23/(2021)* vol. TEAT-7272 (available at: <https://portal.research.lu.se/en/publications/multiple-scattering-by-a-collection-of-randomly-located-obstacles-8>)
- [41] Adda-Bedia M, Katzav E and Vella D 2008 Solution of the Percus–Yevick equation for hard disks *J. Chem. Phys.* **128** 184508
- [42] Kristensson G 2015 Coherent scattering by a collection of randomly located obstacles - an alternative integral equation formulation *J. Quant. Spectrosc. Radiat. Transfer* **164** 97–108
- [43] Kristensson G 2016 *Scattering of Electromagnetic Waves by Obstacles* (Mario Boella Series on Electromagnetism in Information and Communication) (SciTech Publishing)
- [44] Gower A L 2021 Acoustic multiple scattering *Github* (available at: <https://github.com/JuliaWaveScattering/MultipleScattering.jl/blob/master/docs/src/math/acoustics.pdf>)
- [45] Gower A L 2022 Multiple scattering of waves *Github* (available at: <https://github.com/JuliaWaveScattering/MultipleScattering.jl/blob/master/docs/src/math/multiplescattering.pdf>)
- [46] Willis J R 2022 Some personal reflections on acoustic metamaterials *Wave Motion* **108** 102834
- [47] Willis J R 2023 Transmission and reflection of energy at the boundary of a random two-component composite *Proc. R. Soc. A* **479** 20220730
- [48] Linton C M and Martin P A 2006 Multiple scattering by multiple spheres: a new proof of the Lloyd–Berry formula for the effective wavenumber *SIAM J. Appl. Math.* **66** 1649–68
- [49] Craster R V, Guenneau S 2012 *Acoustic Metamaterials: Negative Refraction, Imaging, Lensing and Cloaking* (Springer Science & Business Media)
- [50] Reufer M, Rojas-Ochoa L F, Eiden S, Sáenz J J and Scheffold F 2007 Transport of light in amorphous photonic materials *Appl. Phys. Lett.* **91** 17
- [51] Leseur O, Pierrat R and Carminati R 2016 High-density hyperuniform materials can be transparent *Optica* **3** 763–7

- [52] Versluis M, Stride E, Lajoinie G, Dollet B and Segers T 2020 Ultrasound contrast agent modeling: a review *Ultrasound Med. Biol.* **46** 2117–44
- [53] Wu L and Lin Y S 2023 Flexible terahertz metamaterial filter with high transmission intensity and large tuning range for optical communication application *Physica E* **146** 115563
- [54] Kang S, Kwon Y, Lee H, Kim S, Hong J H, Yoon S and Choi W 2023 Tracing multiple scattering trajectories for deep optical imaging in scattering media *Nat. Commun.* **14** 6871
- [55] Vynck K, Pierrat R, Carminati R, Froufe-Pérez L S, Scheffold F, Sapienza R, Vignolini S and Sáenz J J 2023 Light in correlated disordered media *Rev. Mod. Phys.* **95** 045003
- [56] Gower A L and Deakin J 2020 MultipleScatering.jl: a Julia library for simulating, processing, and plotting multiple scattering of waves (available at: github.com/JuliaWaveScattering/MultipleScatteringjl)
- [57] Gower A L 2018 EffectiveWaves.jl: a Julia package to calculate ensemble averaged waves in heterogeneous materials (available at: github.com/JuliaWaveScattering/EffectiveWavesjl)
- [58] Mogensen P K and Riseth A N 2018 Optim: a mathematical optimization package for Julia *J. Open Source Softw.* **3** 615
- [59] Montiel F, Squire V A and Bennetts L G 2016 Attenuation and directional spreading of ocean wave spectra in the marginal ice zone *J. Fluid Mech.* **790** 492–522
- [60] Montiel F, Squire V A and Bennetts L G 2015 Evolution of directional wave spectra through finite regular and randomly perturbed arrays of scatterers *SIAM J. Appl. Math.* **75** 630–51
- [61] Kaipio J P and Somersalo E 2005 *Statistical and Computational Inverse Problems* (Springer)